Use of Power Transform Total Number Concentration as Control Variable for Direct Assimilation of Radar Reflectivity in GSI En3DVar and Tests with Six Convective Storms Cases

HUIQI LI,[a,b] CHENGSI LIU,[a] MING XUE,[a,c] JUN PARK,[a] LIANGLYU CHEN,[d,a] YOUNGSUN JUNG,[a] RONG KONG,[a] AND CHONG-CHI TONG[a]

[a] *Center for Analysis and Prediction of Storms, University of Oklahoma, Norman, Oklahoma*
[b] *Institute of Tropical and Marine Meteorology, China Meteorological Administration, Guangzhou, China*
[c] *School of Meteorology, University of Oklahoma, Norman, Oklahoma*
[d] *Chongqing Institute of Meteorological Sciences, Chongqing, China*

(Manuscript received 3 March 2021, in final form 11 January 2022)

ABSTRACT: When using a double-moment microphysics scheme, both hydrometeor mixing ratios and number concentrations are part of the state variables that are needed to initialize convective-scale forecasting. In the Thompson microphysics scheme, both mixing ratio and total number concentration of rainwater (N_{tr}) are predicted and they are also involved in the reflectivity observation operator. In such a case, when directly assimilating reflectivity using N_{tr} as the control variable (denoted as CVnr) within a variational framework, the large dynamic range of N_{tr} and the nonlinear relationship between reflectivity and N_{tr} prevent efficient minimization convergence. Using logarithmic N_{tr} as the control variable (CVlognr) alleviates the problem to some extent but can produce spurious analysis increments in N_{tr}. In this study, a general power transform of N_{tr} is proposed as the new control variable for N_{tr} (CVpnr) where the nonlinearity of transform can be adjusted by tuning the exponent parameter. This formulation is implemented within the Gridpoint Statistical Interpolation ensemble-3DVar system. The performance of CVpnr with an optimal exponent parameter value of 0.4 is compared with those of CVnr and CVlognr for the analysis and prediction of a supercell case of 16 May 2017 in more detail. CVpnr with optimal exponent yields faster convergence of cost function minimization than CVnr. Subjective and objective evaluations of analyzed and predicted reflectivity and hourly precipitation indicate that the optimized CVpnr outperforms the other two methods. When applied to five additional cases from May 2017, overall statistics show that CVpnr produces generally superior forecasts and is therefore the preferred choice.

KEYWORDS: Radars/Radar observations; Data assimilation; Numerical weather prediction/forecasting

1. Introduction

Radar data including radial velocity (V_r) and reflectivity (Z) can provide detailed information about the internal structures of storms at high spatial and temporal resolutions, which is critical for convective-scale analysis and forecast. Numerous studies have demonstrated the positive impacts of assimilating radar observations (e.g., Sun and Crook 1997, 1998; Xue et al. 2003; Dowell et al. 2004; Tong and Xue 2005; Dawson and Xue 2006; Hu et al. 2006; Gao and Xue 2008; Yussouf and Stensrud 2010; Schenkman et al. 2011; Snook et al. 2011, 2012; Sun et al. 2013; Wang et al. 2013; Yussouf et al. 2013; Wang and Wang 2017; Tong et al. 2020; Kong et al. 2021). However, direct assimilation of radar Z remains challenging, owing to the high nonlinearity of its observation operator and the complex microphysics (MP) involved.

The ensemble Kalman filter (EnKF; Evensen 1994, 2003) is attractive for directly assimilating radar Z at the convective scale because flow-dependent error covariance statistics derived from the forecast ensemble can be used to update unobserved model state variables. Moreover, EnKF does not require tangent linear and adjoint of the observation operator as variational approach does, so the highly nonlinear Z observation operator that is often linked to a complex, multicategory, multimoment MP scheme can be more easily implemented. Many studies have demonstrated the potential of EnKF in radar data assimilation (DA) at convective scale (e.g., Tong and Xue 2005; Jung et al. 2008, 2012; Dowell et al. 2011; Snook et al. 2011, 2012; Yussouf et al. 2013; Johnson et al. 2015; Labriola et al. 2017, 2020; Tong et al. 2020). However, insufficient ensemble spread and low-rank ensemble background error covariance due to a small ensemble size are main causes of suboptimal performance. For example, the background error cannot be corrected in the area where precipitation is observed but no ensemble member predicts precipitation. Furthermore, the non-Gaussianity of the background and observation errors violates the assumption in EnKF and results in a suboptimal analysis (Lorenc 2003).

Using a hybrid ensemble–variational (EnVar) method that combines static and ensemble-derived flow-dependent background error covariance within variational framework (Hamill and Synder 2000; Lorenc 2003) can somewhat alleviate the aforementioned problems in EnKF, and has

Jung's current affiliation: NOAA/NWS/Office of Science and Technology Integration, Silver Spring, Maryland.

Corresponding author: Chengsi Liu, cliu@ou.edu

DOI: 10.1175/MWR-D-21-0041.1

shown promise for convective-scale DA (e.g., Gao et al. 2013; Gao and Stensrud 2014; Kong et al. 2018, 2021; Wang et al. 2019; Tong et al. 2020). However, when directly assimilating radar Z within variational DA framework, the high nonlinearity of Z observation operator can cause various issues (Sun and Crook 1997; Carley 2012; Wang and Wang 2017; Liu et al. 2020). Liu et al. (2020) investigated such issues when mixing ratio (CVq) or logarithmic mixing ratio is used as the control variable (CVlogq) to assimilate Z, and proposed several treatments to allow for the proper assimilation of Z data.

Even though much progress has been made for using EnKF and hybrid EnVar to assimilate radar Z, few studies have focused on the use of a Z observation operator consistent with the multimoment MP scheme that is used in the forecast model. Bulk MP schemes are commonly used in numerical weather prediction models to parameterize cloud and precipitation processes using a semiempirical function of particle size distribution, such as the gamma distribution. Single-moment (SM) bulk MP schemes (e.g., Lin et al. 1983; Kessler 1995) typically assume that the particle size distribution for each hydrometeor category has a generalized gamma distribution with fixed intercept and shape parameters, and they predict the hydrometeor mixing ratios that are proportional to the corresponding slope parameter of particle size distribution. Double-moment (DM) MP schemes typically predict both mixing ratios and total number concentrations so that the intercept and slope parameters can be determined and change independently (e.g., Thompson et al. 2004; Milbrandt and Yau 2005). Several studies have shown that using DM MP schemes, some within the EnKF framework, can produce more realistic structure and evolution of convective storms, and better prediction for supercell and mesoscale convective systems than using SM MP schemes (e.g., Jung et al. 2010a; Dawson et al. 2010; Jung et al. 2012; Putnam et al. 2014; Johnson et al. 2016; Labriola et al. 2017).

When using a variational method to assimilate Z, due to the need for the adjoint of its observation operator, most previous studies adopted a Z operator, which is based on a SM MP scheme and the DA system only updated hydrometeor mixing ratios (e.g., Sun and Crook 1997; Gao and Stensrud 2012; Kong et al. 2018; Liu et al. 2019). Recently, Liu et al. (2022) implemented a Z observation operator (together with its adjoint) based on the DM Thompson MP scheme (Thompson et al. 2008) within the Gridpoint Statistical Interpolation (GSI; Kleist et al. 2009) hybrid En3DVar system for direct assimilation of Z data. Their results show that using the DM-type Z operator in hybrid En3DVar outperforms using the SM-type Z operator for the forecast of convective storms when the Thompson MP scheme is used in the forecast model. With the implementation, the total number concentration of rainwater is used as a control variable (among the precipitating hydrometeors the Thompson scheme only predicts two moments for rainwater and cloud ice; because the contribution from cloud ice to the total reflectivity is relatively small, it is not considered in the present Z observation operator). However, the very large dynamic range of total number concentration (which varies by several orders of magnitude) and associated nonlinearity do pose challenges and impact Z assimilation, an issue not investigated in Liu et al. (2022). A logarithmic transformation can be used to reduce the dynamic range of the variable but can lead to insensitivity to large values (Hogan 2007; Tong and Xue 2008; Jung et al. 2010b; Carley 2012; Wang and Wang 2017). Xue et al. (2010) used a simple power transform of total number concentration when assimilating Z data with EnKF in order to reduce the dynamic range of the variable while trying to retain sensitivity at large values. In the NCEP Real Time Mesoscale Analysis system (de Pondeca et al. 2011), Yang et al. (2020) applied a general nonlinear power transform function to ceiling height and visibility which also have wide ranges of variation. Using the power transform can narrow the variable dynamic range and make the distribution of the variable closer to Gaussian, thereby making the linear and Gaussian assumptions within the DA system more valid. In the general nonlinear power transform function, the nonlinearity of transform can be adjusted by tuning an exponent parameter. Chen et al. (2021) applied this transform to hydrometeor mixing ratios and used them as the new control variables (CVpq) when assimilating Z data within GSI En3DVar. Their results show that CVpq with a tuned power parameter outperforms CVq and CVlogq. However, due to the unavailability of a Z operator (in particular its adjoint) consistent with the Thompson MP scheme in GSI EnVar at the time, they used a Lin-type SM MP Z operator in GSI EnVar while the Z operator based on the Thompson MP scheme is used in GSI EnKF so that this inconsistency introduces additional error. In addition, the SM MP Z operator itself is not directly linked to the additional state variables such as the total number concentrations when a DM MP scheme is used. In such systems, only the hydrometeor mixing ratios are updated even though the total number concentration also directly affects Z.

In this study, we extend the work of Chen et al. (2021) and Liu et al. (2022) by applying the general nonlinear power transform proposed in Chen et al. (2021) to the total number concentration of rainwater (N_{tr}) that is also part of the Thompson MP scheme, and use such a transformed control variable (hereafter referred to as CVpnr) to assimilate Z data with the Thompson Z observation operator developed by Liu et al. (2022). Our focus is to investigate the impacts of CVpnr on the analysis and forecast of convective storms. CVpnr with a selected exponent parameter is compared with the use of N_{tr} or logarithmic N_{tr} as control variable (referred to as CVnr and CVlognr, respectively) for six thunderstorm cases during May 2017. Among these cases, a high-impact case of supercells over Texas and Oklahoma on 16 May 2017 is used to examine the performance of CVpnr in greater detail.

The rest of this paper is organized as follows. The GSI En3DVar system, the radar observation operators and the nonlinear power transform function are introduced in section 2. Section 3 describes the experiment configurations. Section 4 presents and discusses the results from the analysis and forecast experiments. A summary and conclusions are given in the final section. A list of acronyms/symbols and their definitions can be found in the appendix.

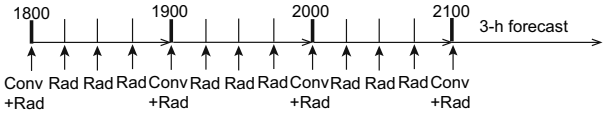

FIG. 1. The flowchart of the cycled data assimilation and 3-h forecast experiments.

2. Methodology

a. GSI pure En3DVar algorithm

All experiments in this study are conducted using the GSI En3DVar DA system, and utilize the pure En3DVar algorithm that employs 100% ensemble-derived background error covariance as in Chen et al. (2021). The extended control variable approach of Lorenc (2003) is adopted in the implementation of the GSI En3DVar system (Kleist and Ide 2015). A brief description of the algorithm below follows Pan et al. (2014) but omits the static background term in the cost function.

Within the pure En3DVar framework, the analysis increment $\delta\mathbf{x}$ can be obtained by minimizing the following cost function:

$$J(\mathbf{a}) = \frac{1}{2}\mathbf{a}^{\mathrm{T}}\mathbf{A}^{-1}\mathbf{a} + \frac{1}{2}\left(\mathbf{H}\delta\mathbf{x} - \delta\mathbf{y}^{O}\right)^{\mathrm{T}}\mathbf{R}^{-1}\left(\mathbf{H}\delta\mathbf{x} - \delta\mathbf{y}^{O}\right). \quad (1)$$

Here $\mathbf{A}$ is a block-diagonal matrix defining the ensemble covariance localization (Lorenc 2003; Wang et al. 2007), and the vector $\mathbf{a}$ is the control variables. The term $\delta\mathbf{y}^{o} = \mathbf{y}^{o} - H(\mathbf{x}^{b})$ is the observation innovation vector where H is the observation operator and $\mathbf{x}^{b}$ is the background state vector. The variable $\mathbf{H}$ is the linear approximation to H and $\mathbf{R}$ is the observation error covariance.

b. Radar radial velocity and reflectivity observation operators

Both radar radial velocity and reflectivity observations are directly assimilated within the GSI variational framework. The observation operator for V_r is

$$V_r = u\sin\varphi\cos\mu + \upsilon\cos\varphi\cos\mu + w\sin\mu, \quad (2)$$

where u, υ, and w represent zonal, meridional, and vertical velocity, respectively. The term φ is the azimuth angle, and μ is elevation angle of radar beams.

The reflectivity observation operator used in this study is newly developed by Liu et al. (2022) based on the DM Thompson MP scheme. The reflectivity can be written as

$$Z = 10\log_{10}(Z_e), \quad (3)$$

where Z_e is the equivalent radar reflectivity factor containing the contributions from three types of hydrometeors: rainwater, snow, and graupel, which can be written as follows:

$$Z_e = Z_{er} + Z_{es} + Z_{eg}. \quad (4)$$

In Eq. (4), Z_{er}, Z_{es}, and Z_{eg} are the equivalent radar reflectivity factors of rainwater, snow, and graupel, respectively.

The Thompson scheme predicts two moments for rainwater (and cloud ice) while a single moment is predicted for other hydrometeors. In the observation operator employed in this study, the rainwater component for the Thompson scheme has the following form:

$$Z_{er} = \frac{720 \times (\rho q_r)^2 \times 10^{18}}{\pi^2 \rho_r^2 N_{tr}}, \quad (5)$$

where ρ is the air density, ρ_r is the rainwater density and N_{tr} is the total number concentration of rainwater which can be updated as well as the rainwater mixing ratio (q_r). When the DM Thompson MP scheme is used in the forecast model, both q_r and N_{tr} should be properly initiated for the convective-scale forecasting, Therefore, N_{tr} should be included as a control variable and updated together with q_r by the DA system. Otherwise, the inconsistency may lead to additional error.

For snow component, the snow size distribution assumes a combination of the exponential and gamma distributions and the density is a function of the particle diameter. To simplify the snow reflectivity formula for the tangent linear and its adjoint models, the simulated snow reflectivity (Z_s) is fit to a power-law form of snow mixing ratio (q_s), resulting in the following relation:

$$Z_s = 16.02 \times q_s^{0.56}. \quad (6)$$

TABLE 1. A brief description of the experiments for the 16 May 2017 case in this study.

Expt	Description	Expt	Outer loops (inner loops)
Cycled DA and forecast experiments	Follow the flowchart in Fig. 1.	CVnr	3 (25)
		CVpnr0.2	3 (25)
		CVpnr0.4	3 (25)
		CVpnr0.6	3 (25)
		CVpnr0.8	3 (25)
		CVlognr	3 (25)
Single-time analysis experiments	Conduct single-time analyses using the same background at 2000 UTC 16 May 2017	CVnr	3 (25)
		CVpnr0.4	3 (25)
		CVlognr	3 (25)
		CVnr_O5I200	5 (200)
		CVpnr0.4_O5I200	5 (200)
		CVlognr_O5I200	5 (200)

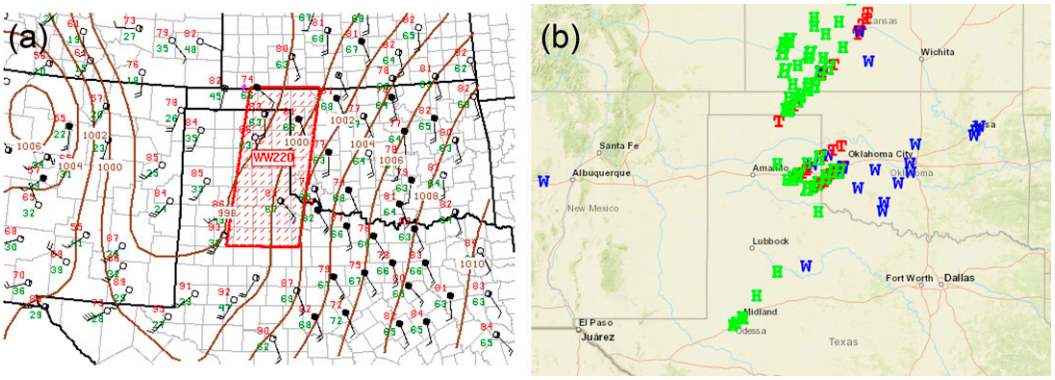

FIG. 2. (a) Mesoscale analysis issued at 2036 UTC 16 May 2017 and (b) storm reports for 16 May 2017 from the Storm Prediction Center (SPC). The red box marked WW20 is the region for tornado watch issued by the Storm Prediction Center. Letters "T," "H," and "W" in (b) denote tornado, hail, and wind reports, respectively.

In the Thompson scheme, although the graupel process uses a SM parameterization, the intercept parameter for graupel is diagnosed as a function of its mixing ratio (Thompson et al. 2008). The forward operator for graupel is given as

$$Z_{eg} = \frac{10^{18} \times (\rho \times q_g)^{1.75} \times 720}{\pi^{1.75} \times \left(\frac{200}{q_g \times 0.02}\right)^{0.75} \times {\rho_g}^{1.9}}, \tag{7}$$

where ρ is the air density, ρ_g is the graupel density, and q_g is the graupel mixing ratio.

A complete description and derivation of the Z observation operator can be found in Liu et al. (2022). The control variables used in the experiments in this study include streamfunction, potential velocity function, surface pressure, temperature, water vapor mixing ratio, q_r, N_{tr}, q_s, q_g, and vertical velocity.

c. *Power-transformed total number concentration of rainwater as control variable (CVpnr)*

The nonlinear power transform proposed by Yang et al. (2020) and utilized for mixing ratios in Chen et al. (2021) is applied to N_{tr}, and the transformed variable $\hat{N}_{tr}$ is used as part of the control variable in the cost function. The transform function is as follows:

$$\hat{N}_{tr} = (N_{tr}^{p} - 1)/p, \tag{8}$$

where p is an adjustable parameter. It is mathematically a power law function. In practice, p value is limited to the range $0 < p \leq 1$. When $p \to 0$, the function approaches the natural logarithm function so that CVpnr is effectively the same as CVlognr. When the p value increases, the nonlinearity of Eq. (8) decreases. When $p = 1$, the function becomes a linear function, i.e., CVpnr becomes equivalent to CVnr.

3. Experiment configurations

In this study, version 3.8.1 of Weather Research and Forecasting (WRF) Model is used as the forecast model. The model domain follows the National Severe Storms Laboratory Experimental Warn-on-Forecast (WoF) System (Wheatley et al. 2015), and is centered on the location of the severe weather event, using 250 × 250 grid points in the horizontal with a 3-km grid spacing and 50 vertical levels. The following model

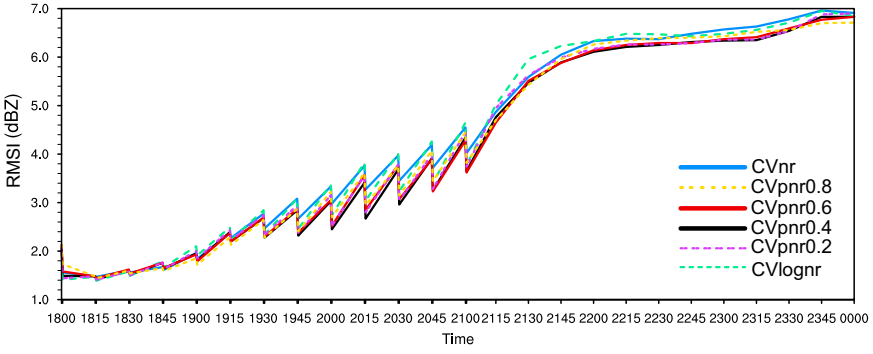

FIG. 3. RMSI for reflectivity of cycled data assimilation and 3-h forecasts using different forms of N_{tr} as the control variable. "CVnr" and "CVlognr" in the legend indicate using CVnr and CVlognr, respectively; "CVpnr0.4" indicates using CVpnr with p set to 0.4; similarly for the rest of the figures.

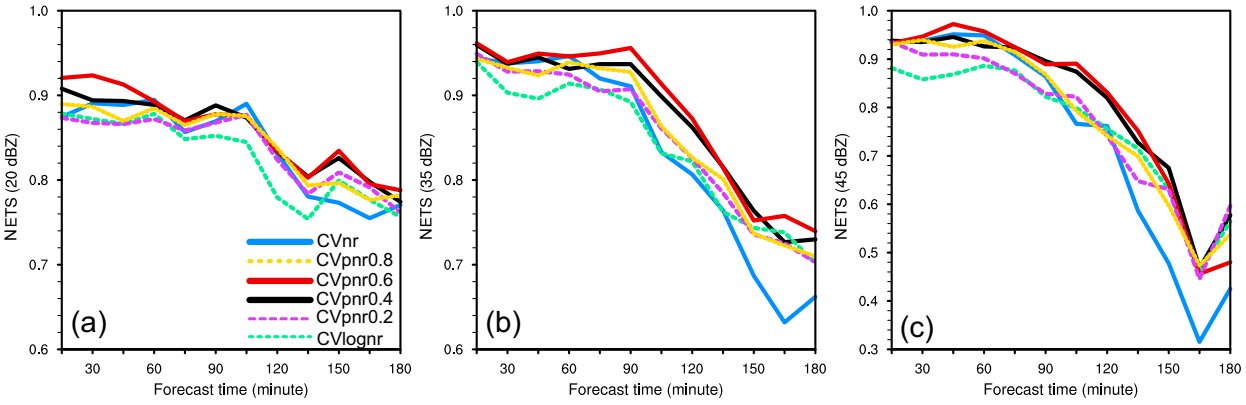

FIG. 4. NETSs for thresholds of (a) 20, (b) 35, and (c) 45 dBZ for 3-h composite reflectivity forecasts using different forms of N_{tr} as the control variable.

physical schemes are employed: the Thompson microphysics scheme (Thompson et al. 2008), the RRTMG shortwave and longwave schemes (Iacono et al. 2008), the Yonsei University (YSU) planetary boundary layer scheme (Hong et al. 2006), and the unified Noah land surface model (Chen and Dudhia 2001). All experiments are initialized at 1800 UTC with initial and lateral boundary conditions provided by the High-Resolution Rapid Refresh Ensemble (HRRRE; Dowell et al. 2016). More specifically, the initial conditions are taken from 1-h 36-member HRRRE forecasts launched at 1700 UTC. DA is conducted using GSI En3DVar system (based on ProdGSI of August 2019). The ensemble perturbations required by En3DVar are taken from GSI EnKF run in parallel, i.e., via a one-way EnKF–En3DVar coupling approach (Pan et al. 2014; Kong et al. 2018). The EnKF DA cycles of the same length are run independently of the En3DVar while providing ensemble perturbations to En3DVar and both systems assimilate the same observations. Conventional data (e.g., surface stations, buoys, soundings), radar reflectivity and radial velocity observations are assimilated. Gridded radar reflectivity observations from the Multi-Radar Multi-Sensor (MRMS; Smith et al. 2016) system are interpolated to the locations of the model grid horizontally with a resolution of 3 km but remain at the 33 vertical levels with a resolution of 500 m. Radial velocity V_r observations are processed from the WSR-88D Level-2 data using a quality control and processing procedure from a procedure of the Advanced Regional Prediction System (Brewster et al. 2005). The V_r data are interpolated to the model grid column locations horizontally but kept on the radar elevation levels without interpolation in the vertical for each radar site (including KAMA, KDDC, KDYX, KFDR, KFDX, KFWS, KICT, KINX, KLBB, KTLX, KTWX, and KVNX). No further data thinning on the grid is employed here. The Z and V_r observation errors are, respectively, assumed to be 5 dBZ and 1 m s^{-1}, which contain the instrument and representation error information of radar. In the EnKF, the horizontal and vertical localization radii for conventional (radar) data are 300 (12) km and 0.4 (0.7) scale height, respectively, which have been tested and recommended by Labriola et al. (2021). Effectively the same localization radii of EnKF are also used by En3DVar, where the cutoff radii of EnKF are converted to equivalent recursive filter decorrelation length scales (Pan et al. 2014).

For the DA cycles and forecast experiments, radar observations are assimilated every 15 min and conventional observations are assimilated hourly between 1800 and 2100 UTC. The 3-h forecasts are launched at 2100 UTC (Fig. 1). The 3-h forecasts are conducted because the WoF aims at providing short-term (0–3 h) forecasts for severe convective storms and their hazards (Stensrud et al. 2009; Wheatley et al. 2015). Several experiments are performed using the nonlinear power transform in Eq. (8) with different p values. The experiment with $p = 10^{-6}$ approximates CVlognr while $p = 1$ corresponds

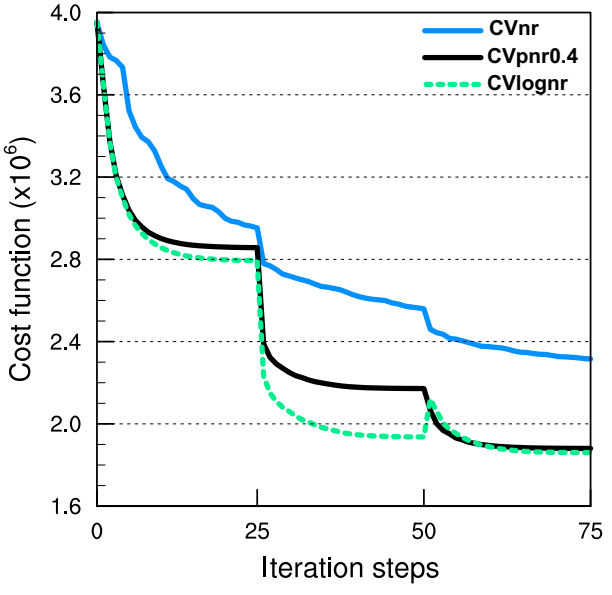

FIG. 5. Cost function with respect to the total number of iterations accumulated in three outer loops (25 iterations each) for CVnr (blue), CVpnr0.4 (black), and CVlognr (green) at analysis time 2000 UTC 16 May 2017.

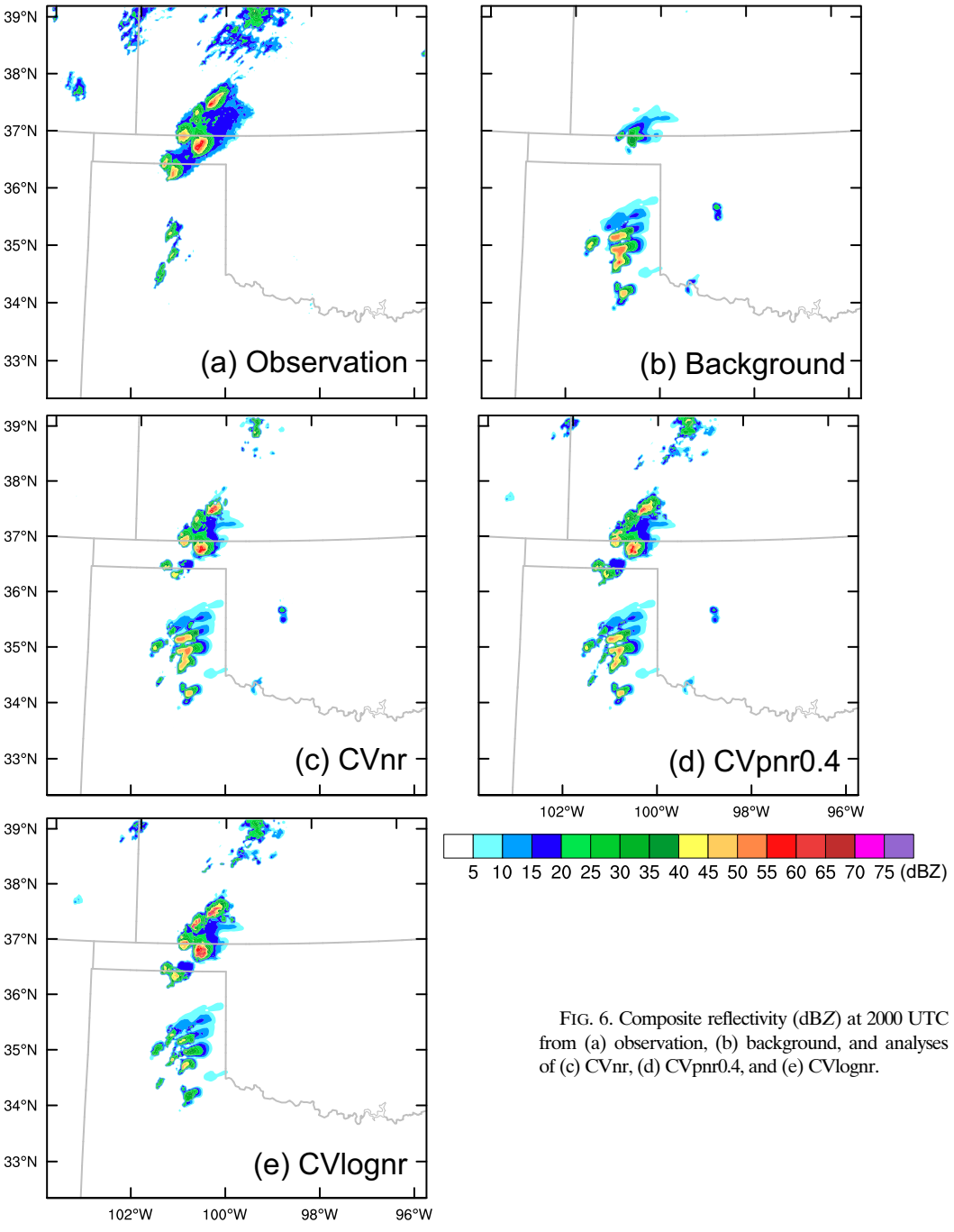

FIG. 6. Composite reflectivity (dBZ) at 2000 UTC from (a) observation, (b) background, and analyses of (c) CVnr, (d) CVpnr0.4, and (e) CVlognr.

to CVnr. Following Chen et al. (2021), the nonlinear power transform is also applied to hydrometeor mixing ratios with p set to 0.4 in all experiments. To highlight the differences in convergence of cost function minimization among these forecast experiments, 3 outer loops are used with 25 iterations for the inner loop unless otherwise specified (Table 1). The convergence criterion is set in terms of the norm of gradient. The experiments are performed for six convective cases of central United States from May 2017 and the results with different p values are compared.

4. Results

In this section, the impact of using CVpnr on the analysis and forecast of thunderstorms is first examined for a high-impact supercell case over Texas and Oklahoma on 16 May 2017. For CVpnr, an optimal value of p is first determined by running experiments for this case with different p values, and the results of CVpnr using this optimal value will then be compared with CVnr and CVlognr in more detail. In the last subsection, the performances of CVpnr with optimal p, CVnr and CVlognr in cycled DA and forecast experiments

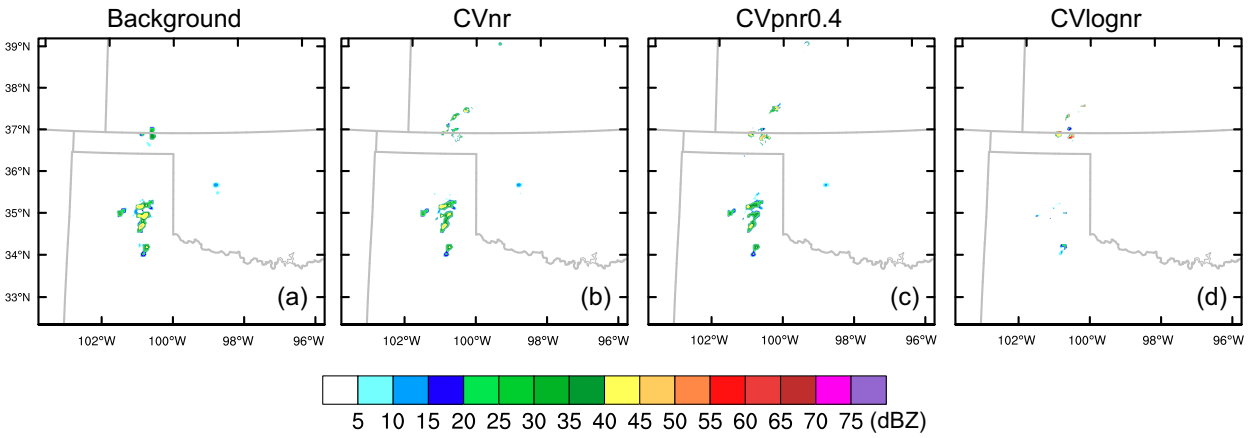

FIG. 7. Reflectivity contributed by rainwater at 2 km MSL at 2000 UTC, from (a) background, and single-time analyses of (b) CVnr, (c) CVpnr0.4 (c), and (d) CVlognr.

are statistically evaluated for six May 2017 thunderstorm cases.

a. Results for the supercell case of 16 May 2017

On 16 May 2017, several convective storms were initiated along a dryline near the Texas Panhandle area where environmental conditions were favorable for tornadoes and large hail (Fig. 2a). Around 1800 UTC, some storms were initiated in the northern Texas Panhandle and then moved northeastward across the west–east-oriented Texas–Oklahoma border, producing at least two tornadoes and golf-ball- to hen-egg-sized hail in that region (Fig. 2b). Later, two intense supercells moving from the south of the Texas Panhandle eastward to Oklahoma produced a few tornadoes and large hail. A damaging tornado was reported to hit Elk City, Oklahoma, around 0035 UTC, causing one fatality and numerous damaged structures (https://www.spc.noaa.gov/climo/reports/170516_rpts.html).

1) RESULTS OF EXPERIMENTS WITH DIFFERENT *P* VALUES

The value of parameter p in Eq. (8) regulates the degree of nonlinearity of the power transform function. Six cycled DA and forecast experiments are conducted using the nonlinear power transform in Eq. (8) with p set to 10^{-6}, 0.2, 0.4, 0.6, 0.8, and 1.0, respectively, for the 16 May case. To determine the optimal p value for CVpnr for further comparison with CVlognr and CVnr, the root-mean-square innovation (RMSI) of Z is calculated for the DA cycles and subsequent 3-h forecasts (Fig. 3). All experiments have similar RMSIs during the first two cycles. For the cycles between 1845 and 1930 UTC, the RMSIs are slightly smaller when p = 0.8 (denoted as CVpnr0.8 as a convention). CVpnr0.4 (with p = 0.4) has the smallest RMSIs during the assimilation period from 1945 to 2030 UTC. After that, CVpnr0.4 and CVpnr0.6 show comparable performance for the DA cycles and subsequent forecasts. It is noted that CVnr and CVlognr have larger RMSIs after 1900 UTC, indicating that the power transform with a medium p value is preferred for Z analysis and forecast.

Neighborhood equitable threat score (NETS; Clark et al. 2010) of Z is further calculated for the 3-h forecasts (Fig. 4). The neighborhood radius is set to 40 km, the same as that used in the verification of the WoF system for convective-scale forecasts (Skinner et al. 2018). NETSs are calculated for composite reflectivity thresholds of 20, 35, and 45 dBZ. For most of the forecast ranges, NETSs at all thresholds for CVpnr0.4 and CVpnr0.6 are higher, except that the NETSs at the 45-dBZ threshold for CVpnr0.6 is next to the lowest at 180 min of forecast. Similar to RMSI, CVnr and CVlognr also have relatively poor performance in NETS. Since CVpnr0.4 generally has the best performance in terms of both RMSI and NETS of forecasts, 0.4 is determined to be the optimal value for p, which happens to also be the optimal value for the power transform of mixing ratios as found in Chen et al. (2021). CVpnr0.4 will therefore be compared with CVnr and CVlognr in more detail in the following subsections.

2) RESULTS OF SINGLE-TIME ANALYSIS EXPERIMENTS

To better understand the performance and impacts of CVnr, CVpnr0.4, and CVlognr on the analysis of thunderstorms, additional experiments are performed assimilating radar data at a single time using the same background (Table 1). To show the impacts more clearly, a relatively poor background at 2000 UTC 16 May is generated as a 30-min forecast from the analysis of cycled DA, assimilating conventional data and radar data with CVnr method every 60 and 30 min, respectively. The only difference among these single-time analysis experiments is the form of the control variable N_{tr} when assimilating radar data at 2000 UTC. The ensemble perturbations are provided by the same EnKF cycles described in section 3. The use of the same background allows us to see better the direct impact of assimilating Z data.

Since one of the motivations for using the power transform is to address the minimization convergence problem when assimilating Z, the convergence of the cost function is examined first. Figure 5 shows the cost function with respect to the number of iterations accumulated in three outer loops for

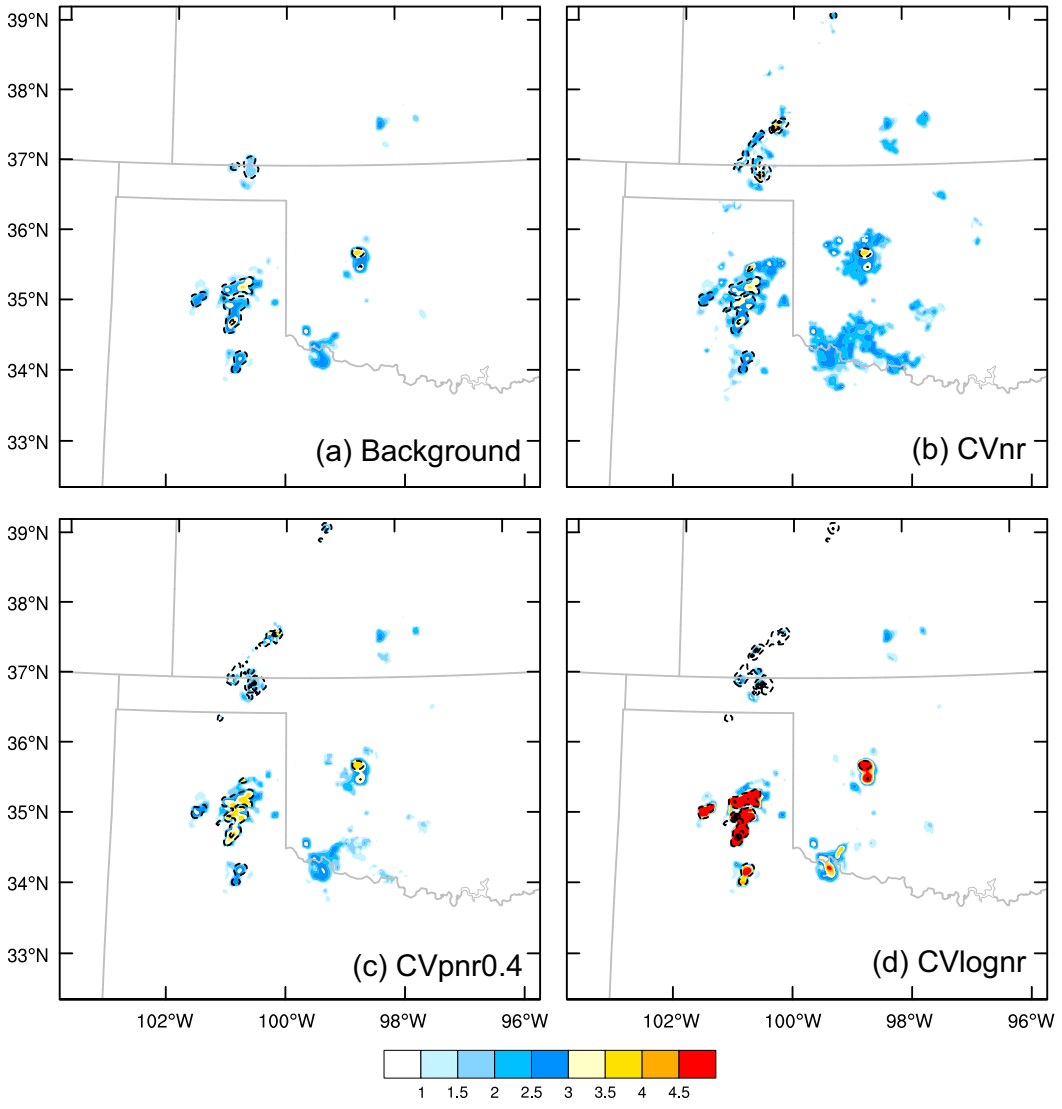

FIG. 8. Mixing ratio (contoured in black starting at 0.01 g kg^{-1} at intervals of 1 g kg^{-1}) and total number concentration (shading; $\log_{10}$ scale) of rainwater at 2 km MSL at 2000 UTC from (a) background, and single-time analyses of (b) CVnr, (c) CVpnr0.4, and (d) CVlognr.

CVnr, CVpnr0.4, and CVlognr. The cost function values of CVpnr0.4 and CVlognr decrease much more rapidly than those of CVnr. At the end of each outer loop (i.e., at the 25th, 50th, and 75th total iteration), the cost function values of CVpnr0.4 and CVlognr no longer change much while cost function curve of CVnr has not flattened yet and is at much higher levels compared to those of CVpnr0.4 and CVlognr. CVpnr0.4 and CVlognr clearly converge much faster than CVnr. In the first and second outer loop, the cost function of CVlognr decreases faster than CVpnr0.4. This may be because the logarithmic transform results in a more linear relationship between Z and the control variables. In the last outer loop, the cost function values of CVpnr0.4 and CVlognr are very similar after a jump in the cost function of CVlognr going from the second to third outer loop. At the end of 75 total iterations, the cost function of CVnr is about 2.3×10^6 versus ~1.85×10^6 of the other two and the cost function reduction rate remains slow.

The composite reflectivity at 2000 UTC from observations, background, and single-time analyses of CVnr, CVpnr0.4, and CVlognr are compared in Fig. 6. As seen in the observation (Fig. 6a), several convective storms are present near the Oklahoma Panhandle and in southwest Kansas while a few other storms are newly initiated in the southern Texas Panhandle (along a dryline). The background evidently underpredicts the storms near the Oklahoma Panhandle and southwest Kansas but predicts earlier development of the southern storms along the dryline (Fig. 6b). All three experiments reproduce the main cells in the north reasonably well (Figs. 6c–e). The weak echo coverage is smaller than observed in all three

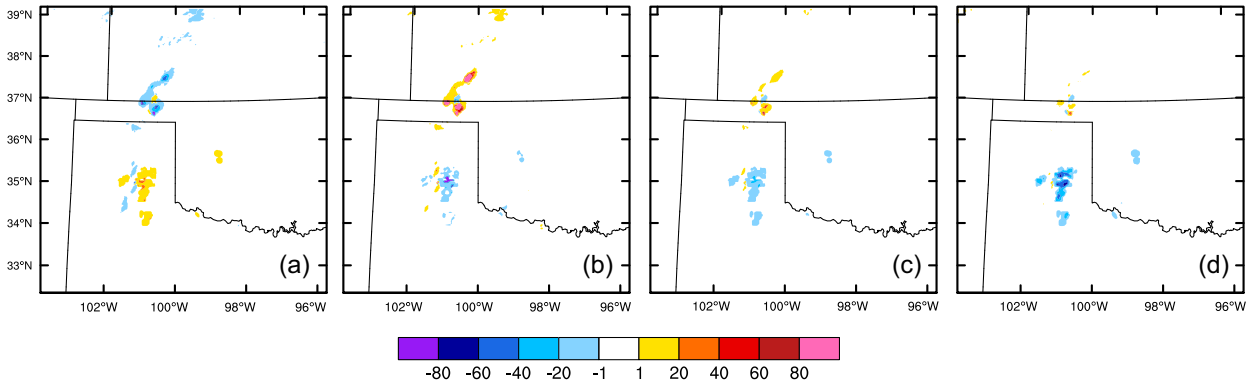

FIG. 9. The gradient of cost function with respect to the control variables (a) power-transformed q_r in the three experiments, (b) N_{tr} in CVnr, (c) power-transformed N_{tr} in CVpnr0.4, and (d) logarithmic transformed N_{tr} in CVlognr, at 2 km MSL at the first iteration step.

experiments, with that of CVnr being the smallest (Fig. 6c), possibly related to the slower minimization convergence discussed earlier, hence a less tight fit to observations. The maximum intensity of the reflectivity core located within the Oklahoma Panhandle is slightly overestimated in CVlognr (Fig. 6e), which is consistent with previous finding that the logarithmic transform may produce spurious analysis increments (Liu et al. 2020). For the northern storms, CVpnr0.4 arguably produces the best reflectivity analysis (Fig. 6d) although the differences are small.

For the southern storms over Texas that are overpredicted in the background (Fig. 6b), both CVnr and CVpnr0.4 only slightly reduce the reflectivity intensity (Figs. 6c,d). It is speculated that larger cost function gradients (with respect to the N_{tr} control variable) at locations of the northern storms dominate the overall cost function when using highly nonlinear Z observation operator (in CVnr and somewhat less in CVpnr0.4) and make variational adjustment for the southern storms less effective, as is the case with V_r DA (together with Z DA) when mixing ratios are directly used as control variables (Liu et al. 2019). CVlognr is able to better suppress the overpredicted echoes with the southern storms (Fig. 6e), though the adjustment to the N_{tr} appears somewhat unphysical, as will be discussed next.

Given that the choice of control variable for N_{tr} has direct impact on the contribution to reflectivity by rainwater (Z_r in dBZ, defined as the logarithmic equivalent reflectivity of rainwater, i.e., $Z_r = 10\log_{10}Z_{er}$), the background and analyzed Z_r at 2 km above mean sea level (MSL) are examined (Fig. 7). Similar to the background composite reflectivity (Fig. 6b), the background Z_r is also underpredicted for the northern storms, but overpredicted in the southern part of the Texas Panhandle. For the northern storms, the analyzed Z_r in all experiments are higher than the background Z_r. In the Oklahoma Panhandle, CVpnr0.4 produces higher Z_r than CVnr in the storm area while CVlognr produces Z_r values of over 55 dBZ that appears to be overestimation. The spurious Z_r in the Texas Panhandle is not effectively suppressed in CVnr or CVpnr0.4 (Figs. 7b,c) but mostly removed in CVlognr (Fig. 7d).

As shown in Eq. (5), both q_r and N_{tr} contribute to Z_r. The q_r and N_{tr} from the background and analyses of CVnr, CVpnr0.4 and CVlognr are compared in Fig. 8. CVnr produces reasonable q_r and N_{tr} increments in the area of northern storms, but more widespread, spurious N_{tr} increments in central and southern Oklahoma (Fig. 8b). With the increase in the nonlinear degree of power transform (i.e., from CVpnr0.4 to CVlognr), larger q_r increments but smaller N_{tr} increments are shown in the area of northern storms compared to CVnr, which explains the higher Z_r in CVpnr0.4 and CVlognr there (Figs. 8c,d). However, for the spurious southern storms, very large N_{tr} values are produced in CVlognr (Fig. 8d).

In the variational framework, the magnitude of analysis increment in a particular variable is linked to the gradient of cost function with respect to that variable. Figure 9a shows the cost function gradient with respect to the power-

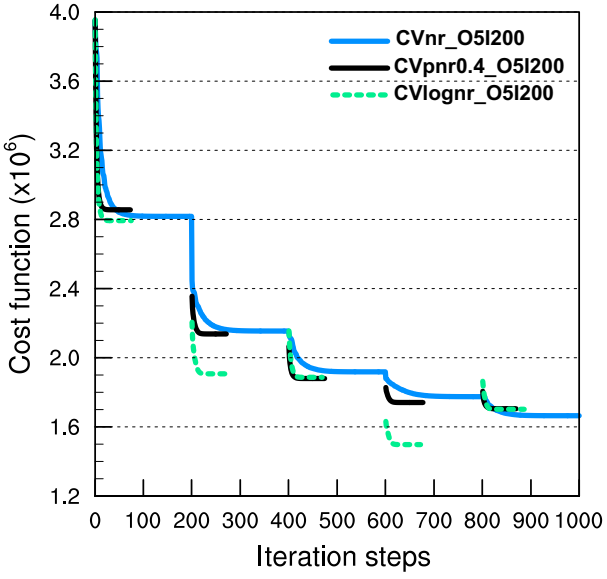

FIG. 10. As in Fig. 5, but for experiments using 5 outer loops and up to 200 inner loops.

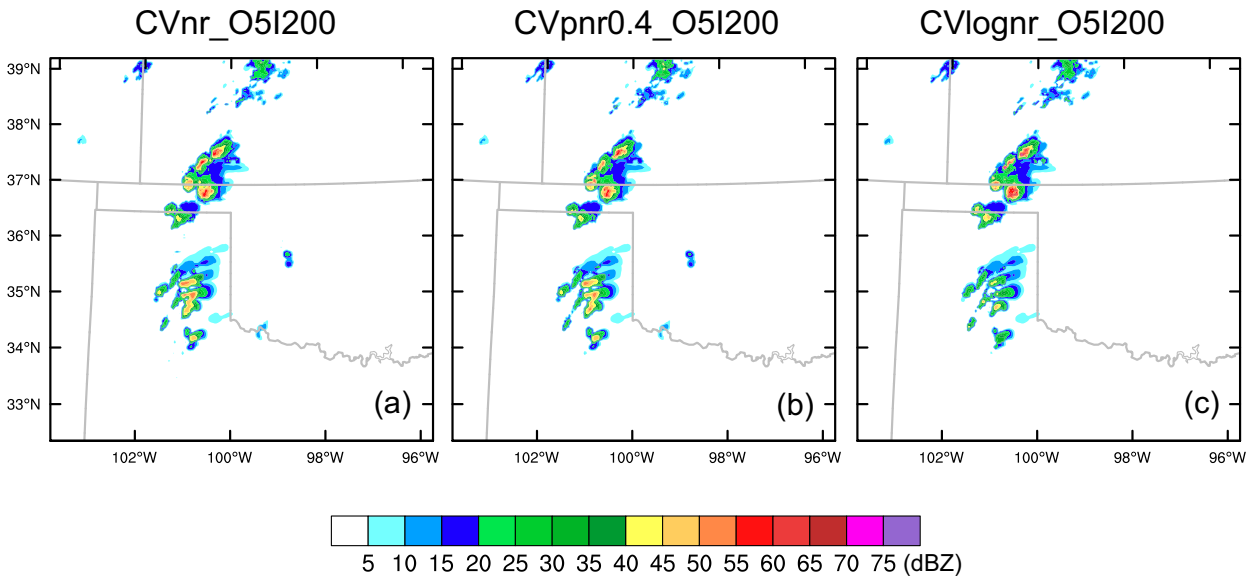

FIG. 11. As in Fig. 6, but for experiments using 5 outer loops and up to 200 inner loops.

transformed q_r control variable (referenced as GDq) at the first iteration step. It should be noted that GDq at the first iteration step is identical in CVnr, CVpnr0.4 and CVlognr because the same power transform of mixing ratios is used in all experiments. Figures 9b–d show the cost function gradient with respect to control variable N_{tr} in CVnr, power-transformed N_{tr} in CVpnr0.4, and logarithmic transformed N_{tr} in CVlognr (these cost function gradients are collectively referenced as GDn for brevity). In CVnr and CVpnr0.4 (Figs. 9a–c), the magnitudes of both GDq and GDn in the area of northern storms are larger than those in the southern Texas Panhandle, resulting in less adjustment for the spurious southern storms. GDn in the area of northern storms generally decreases when increasing nonlinear degree of power transform (i.e., from CVnr to CVlognr, Figs. 9b–d). In CVlognr experiment (Fig. 9d), GDn is rather large over the area of spurious storms in the Texas Panhandle, leading to more adjustment to N_{tr} there. It is noted that small adjustment to $\log(N_{tr})$ can be greatly amplified when the increment is converted back to that of N_{tr}. Therefore, the relatively large cost function gradient with respective to $\log(N_{tr})$ (Fig. 9d) causes very large increments in N_{tr} (Fig. 8d, which is shown in $\log_{10}$ scale).

One of the reasons for the differences among the three experiments is the convergence rate of cost function minimization. It is of interest to see whether the three methods can produce almost the same results if more outer and inner loops are used. The previous single-time analysis experiments are repeated using 5 outer-loop and up to 200 inner-loop iterations (referenced as CVnr_O5I200, CVpnr0.4_O5I200, and CVlognr_O5I200, respectively). Figure 10 shows that the CVnr_O5I200 experiment has a slower convergence rate. Even though the cost function value of CVnr_O5I200 is very close to that of CVpnr0.4_O5I200 at the end of each outer loop but CVnr_O5I200 does not reach the convergence criterion at 200 inner iterations. In contrast, the minimum cost function values of CVpnr0.4_O5I200 and CVlognr_O5I200 are almost reached by 20th iteration and the convergence criterion is met by around 80th iteration for each outer loop, suggesting that the power transform (including the logarithmic transform) does help speed up the cost function convergence rate significantly. The cost function values at the fifth outer loop become similar for all experiments although the values of CVlognr_O5I200 have significant fluctuations between consecutive outer iterations suggesting positive overshooting in the inner-loop adjustments within the outer loop.

Compared to CVnr with fewer iterations (Fig. 6a), the analyzed composite reflectivity in the area of northern storms is somewhat improved in CVnr_O5I200 (Fig. 11a) but it is overestimated (over 55 dBZ) for the small storm to the north of the Oklahoma–Kansas border due to overestimated q_r (Fig. 12a). The additional iterations make few differences between the analyses of CVpnr0.4_O5I200 (Fig. 11b and Fig. 12b) and CVpnr0.4 (Fig. 6d and Fig. 8c). This is consistent with the above discussions on convergence rate. In general, even with much fewer iterations, CVpnr0.4 can produce analyses of similar quality to those of CVpnr0.4_O5I200 and CVnr_O5I200 that use more iterations. The analyses of CVlognr_O5I200 (Fig. 11c) and CVlognr (Fig. 6e) are also similar, and the problem of very large N_{tr} still remains in CVlognr_O5I200 (Fig. 12c). The latter suggests that the final analysis depends mainly on the choice of control variable and hence the formulation of the nonlinear observation operator, provided that the sufficient cost function convergence is reached.

3) RESULTS OF CYCLED DATA ASSIMILATION AND 3-H FORECAST EXPERIMENTS

With the understanding gained on the differences in behaviors of single-time variational analysis using different number

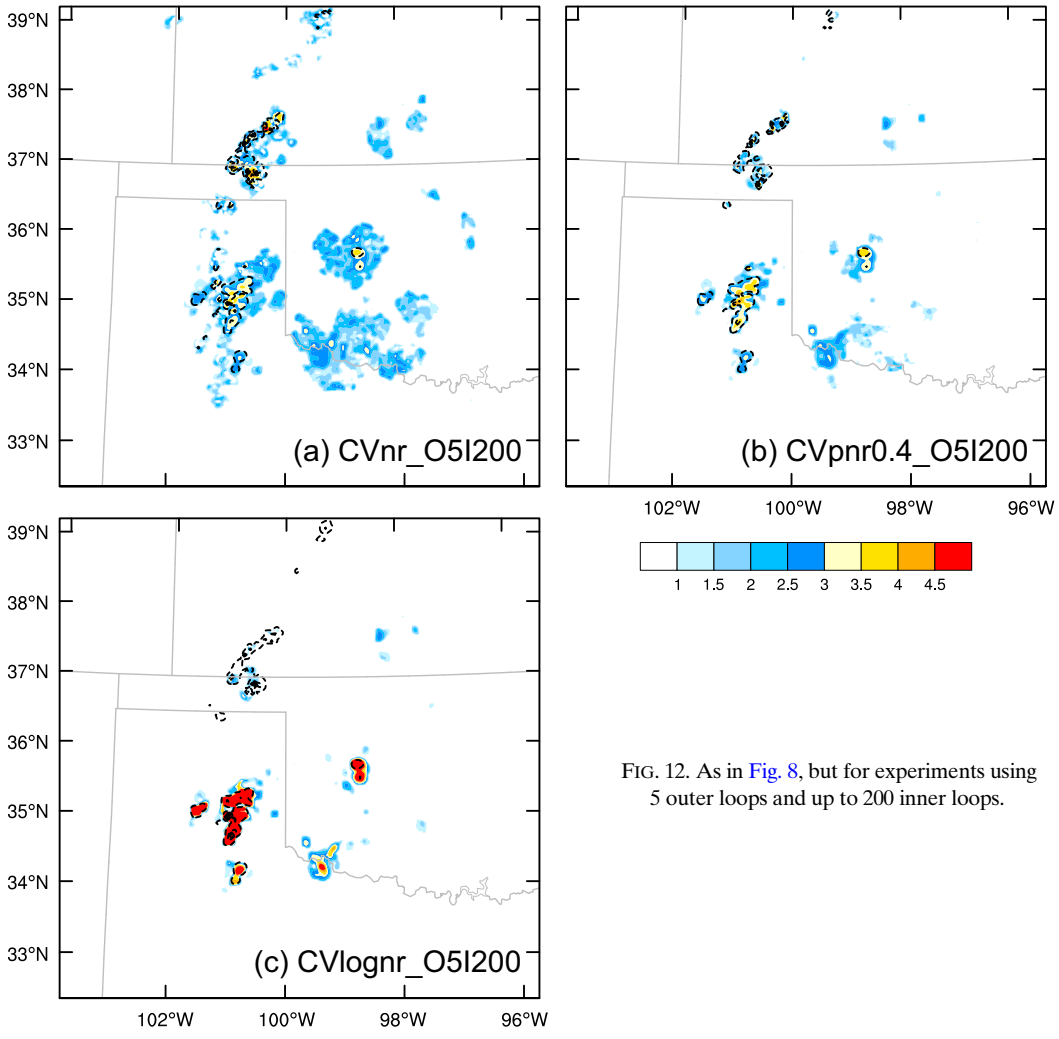

FIG. 12. As in Fig. 8, but for experiments using 5 outer loops and up to 200 inner loops.

concentration control variables with the same background, we examine in this subsection the results of cycled DA and subsequent forecasts for the 16 May case in more detail. The effects of DA formulation differences would accumulate through the DA cycles. As demonstrated earlier in subsection 1), in terms of RMSI and NETS for predicted reflectivity, using power-transformed N_{tr} with a medium value of power parameter p (i.e., CVpnr0.4) generally outperforms CVnr and CVlognr in cycled DA and 3-h forecast experiments. In this subsection, the CVpnr0.4, CVnr and CVlognr will be further compared with additional subjective and objective verifications.

The final analyzed composite reflectivity at 2100 UTC and subsequent predicted composite reflectivity at hourly intervals are compared with the observations in Fig. 13. The observed reflectivity objects over 45 dBZ are captured well in all experiments in the final analyses (Figs. 13b–d) but all experiments produce a line of spurious storms in the eastern part of the Texas Panhandle, mostly east of the correct cells in the region. CVpnr0.4 has fewer/weaker spurious cells than CVnr and CVlognr especially in the northern Texas Panhandle. In the single-time analysis experiment, CVlognr better suppresses the spurious echoes in the region via unphysically large N_{tr} analysis (Fig. 8d). When launching the forecast, the very large N_{tr} quickly decreases (not shown) but more spurious echoes are produced, presumably due to imbalances between the large N_{tr} and other state variables. At the end of DA cycles, CVlognr has more spurious weak echo coverage in the Texas Panhandle and western Oklahoma than other experiments (Fig. 13d) although CVnr has one additional spurious strong echo cell in northeastern corner of the Texas Panhandle (Fig. 13b). Another reason for all final analyses to have the line of spurious cells that are not effectively suppressed through the DA cycles is that the dryline responsible for forcing these cells has eastward position error that is difficult to correct with available surface and radar observations.

In the 1-h forecasts valid at 2200 UTC, the spurious echoes in CVnr and CVpnr0.4 (Figs. 13f,g) are greatly reduced or become more aligned with the observed storms in the eastern part of the Texas Panhandle, but those in CVlognr have become more intense and moved further east into western

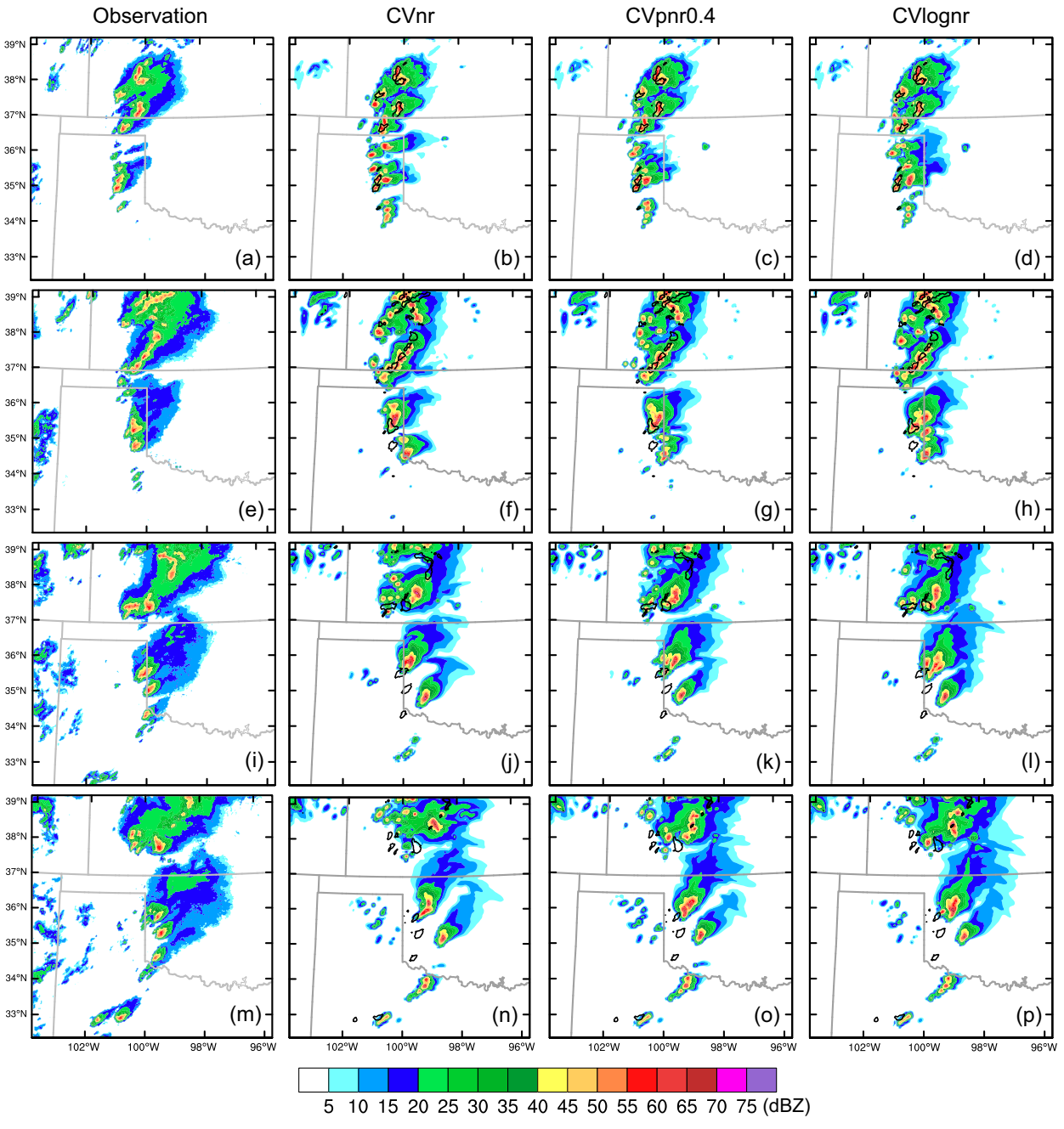

FIG. 13. Composite reflectivity (dBZ) at (a)–(d) 2100, (e)–(h) 2200, and (i)–(l) 2300 UTC 16 May, and (m)–(p) 0000 UTC 17 May from observations, the cycled data assimilation and forecast experiments of CVnr, CVpnr0.4, and CVlognr, shown in columns from left to right. Observed reflectivity exceeding 45 dBZ is contoured in black in the results from cycled data assimilation and forecast experiments (second, third, and fourth columns).

Oklahoma, away from the observed storms (Fig. 13h). All experiments more accurately predict the northeast–southwest-oriented line of convective cells near the Oklahoma–Kansas border but do a poorer job in reproducing the cells further north; the closeness to the model boundary might have played a role. In the 2- and 3-h forecasts, the southern storms in all experiments exhibit an eastward bias (Figs. 13j–l,n–p); they appear to have moved too fast, consistent with the eastward displacement error of the dryline (not shown). However, overall, DA does help reduce the error. Without DA, these storms move even faster and exhibit more distinct eastward bias (not shown).

The hourly precipitation forecasts are plotted against precipitation estimations from MRMS in Fig. 14. While the

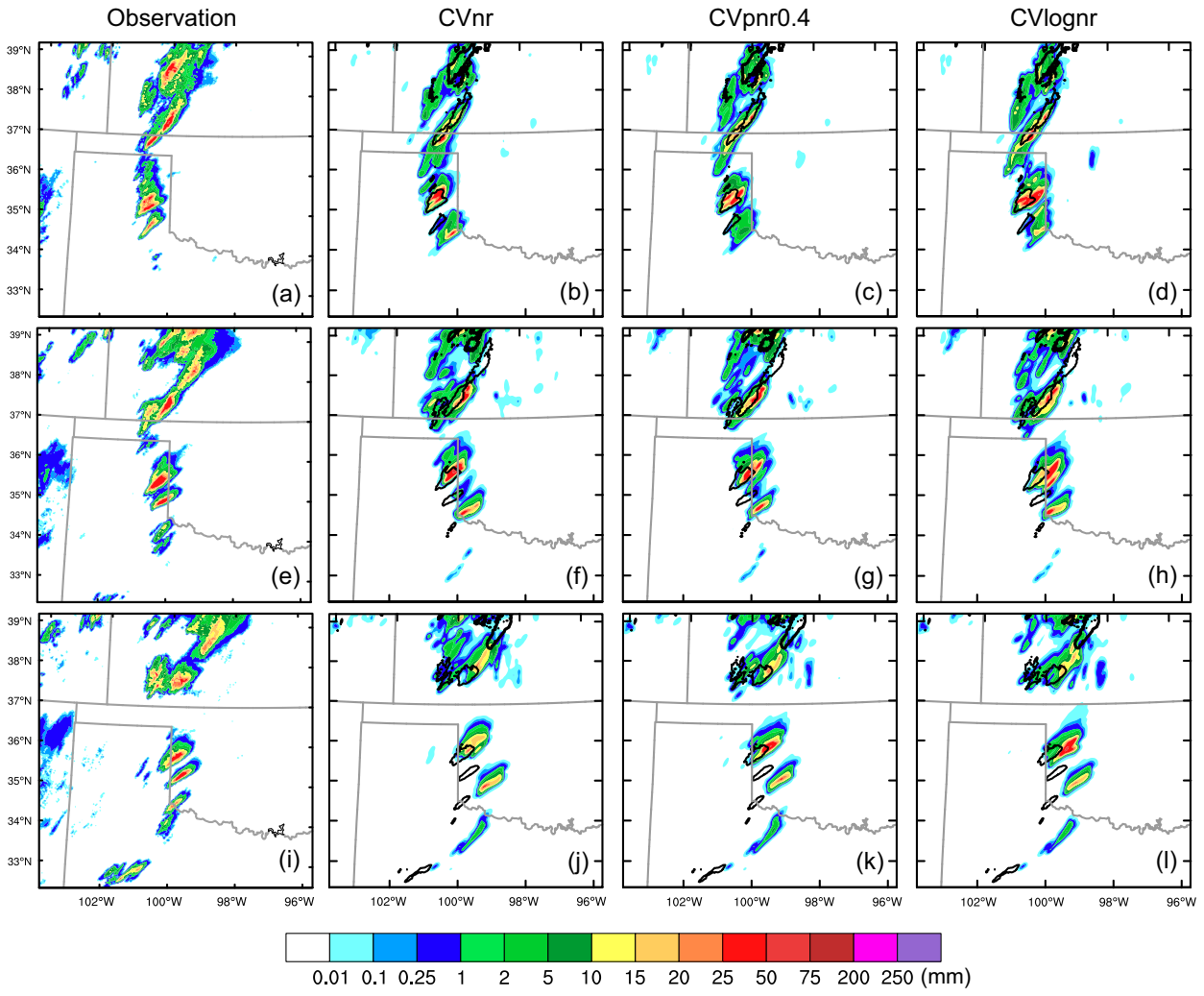

FIG. 14. Hourly precipitation (shading; mm) starting at (a)–(d) 2100, (e)–(h) 2200, and (i)–(l) 2300 UTC 16 May from observations, the cycled data assimilation and forecast experiments of CVnr, CVpnr0.4, and CVlognr, shown in columns from left to right. Observed precipitation exceeding 10 mm is contoured in black in the results from cycled data assimilation and forecast experiments (second, third, and fourth columns).

precipitation in the first forecast hour near the northern boundary of the model domain is underestimated in all experiments (partly because of the orientation of the predicted line of cells that prevents training effect), the band of rainfall near the Oklahoma–Kansas border is accurately predicted in the first hour given the correct orientation and positioning of the line of cells. In the following two hours, the forecasts correctly maintain intense rainfall in the southern part of the band, but fail to predict the northeastward extension, again related to the poorer forecasts to the north. More differences among the three experiments can be seen in the predictions of the precipitation in the Texas Panhandle and western Oklahoma due to cell differences discussed earlier. Both CVnr and CVpnr0.4 quite accurately predict the location and intensity of the northern precipitation center in the first and second hour but exhibit clear northeastward displacement in the third hour, consistent with too fast movement discussed earlier. There is also underprediction in CVnr with this precipitation center in the third hour. CVlognr overpredicts this precipitation center with larger spatial coverage in the first hour and has more eastward displacement than CVnr and CVpnr0.4 in the second and third hour. Therefore, subjectively speaking, CVlognr produces the worse precipitation and storm cell forecasting while that of CVpnr0.4 is slightly better than CVnr.

NETS for hourly precipitation at threshold of 10 mm and a 40-km neighborhood radius is computed to quantitatively evaluate the performance of the three experiments. As shown in Fig. 15, CVpnr0.4 has the highest NETS for the first and last forecast hour, and CVnr has the lowest NETS in the last two forecast hours. The NETS of CVlognr fluctuates during the 3 h, having the lowest skill in the first hour but the highest

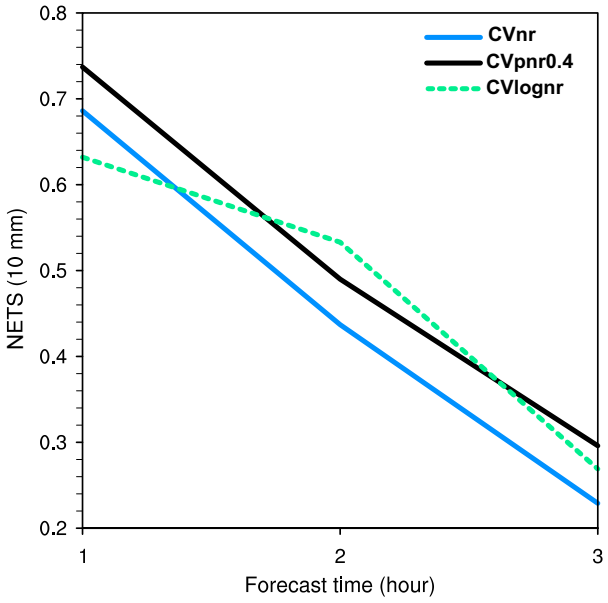

FIG. 15. NETSs for the threshold of 10-mm hourly precipitation forecast for experiments CVnr (blue), CVpnr0.4 (black), and CVlognr (green) for the 16 May 2017 case.

NETS in the second hour. The better skill with CVlognr in the second hour appears to be due to the greater intensity and larger spatial coverage of the eastward displaced precipitation predicted in western Oklahoma, whose position error is tolerated by the neighborhood score. In reality, there is little overlap between the predicted precipitation and observed precipitation in that region (Fig. 14h). Therefore, the qualitative and quantitative evaluations indicate that CVpnr0.4 is more skillful overall for precipitation forecast.

b. *Statistical results for six thunderstorm cases during May 2017*

We have so far performed comparisons and evaluations of analyses and forecasts using different formulations of the rain number concentration control variables for the 16 May 2017 case. To obtain more robust and statistically reliable results, cycled DA and forecast experiments with the same configurations described in section 3 are conducted for five additional thunderstorm cases that occurred in May 2017 (see Table 2 for a list of cases). Among the six cases, three are mostly made up of supercells, and three contained mixed modes of cells and quasi-linear convection. Figures 16a–f present the RMSIs for predicted reflectivity of CVnr, CVpnr0.4, and CVlognr for the six cases during the 3-h forecast period. With the exception of one outlier, the RMSIs of CVpnr0.4 are the smallest for most of the time while those of CVlognr are mostly the largest, especially for the 23 and 27 May cases. The one outlier case, 9 May 2017, has relatively smaller RMSIs compared with other cases and the RMSIs of three experiments are comparable. The RMSIs averaged over the six cases (Fig. 16g) also show that CVpnr0.4 has the best performance while the RMSI of CVlognr at 30 min is substantially larger than others, consistent with the expected larger impacts of initial conditions in earlier hours from DA.

Figures 17 and 18 show the NETSs for predicted composite reflectivity for the 20 and 45-dBZ thresholds, respectively. For the 20-dBZ threshold (Fig. 17), the NETSs of three methods are comparable, and the NETS of CVpnr0.4 becomes generally higher after 105 min except for the 17 May case. In terms of the average NETS (Fig. 17g), CVnr generally has the best performance during the first 60 min. From 60 to 105 min, the NETS of CVpnr0.4 is comparable to that of CVnr but becomes the highest after 105 min. The NETS of CVlognr is overall the lowest, except for 15 min when CVpnr0.4 has lower scores. The differences among the three methods are more evident for the 45-dBZ threshold (Fig. 18). The NETS of CVpnr0.4 is comparable to that of CVnr, and it is higher for most of the time in the 16 and 23 May cases. The NETS of CVlognr is much lower than that of the other two during most of the time. The average NETS (Fig. 18g) of CVnr is slightly lower or comparable to that of CVpnr0.4 during the first 90 min of forecast but drops below that of CVpnr0.4 in the later hours. The poor performance of CVlognr based on the average NETS is consistent with the analysis for each case. CVlognr may produce too large N_{tr}, as seen in the 16 May case, which degrades the forecasts.

Figures 19 and 20 show the performance diagram (Roebber 2009) for predicted composite reflectivity for the 20- and 45-dBZ thresholds, respectively. The performance diagrams provide additional information on the quality of forecasts, including the probability of detection (POD), false alarm ratio (FAR), frequency bias (BIAS), and critical success index (CSI) of reflectivity forecasts. For the 9, 16 and 23 May cases, CVpnr0.4, which has the highest CSI score and less bias for most hours, overall outperforms CVnr and

TABLE 2. List of six selected cases during May 2017. A brief description of primary states affected and storm morphology are provided. Identical DA configurations in the cycled DA and forecast experiments for these cases are also given.

Date	Primary states affected	Storm morphology	DA configurations
9 May	NM, TX	Supercells	CVnr, CVpnr0.4, and CVlognr
16 May	KS, OK, TX	Supercells	(3 outer loops with 25 inner loops)
17 May	IA, IL, MN, WI	Mixed mode of cells and linear convection	
18 May	KS, OK, TX	Supercells	
23 May	TX	Mixed mode of cells and linear convection	
27 May	AR, MO, OK	Mixed mode of cells and linear convection	

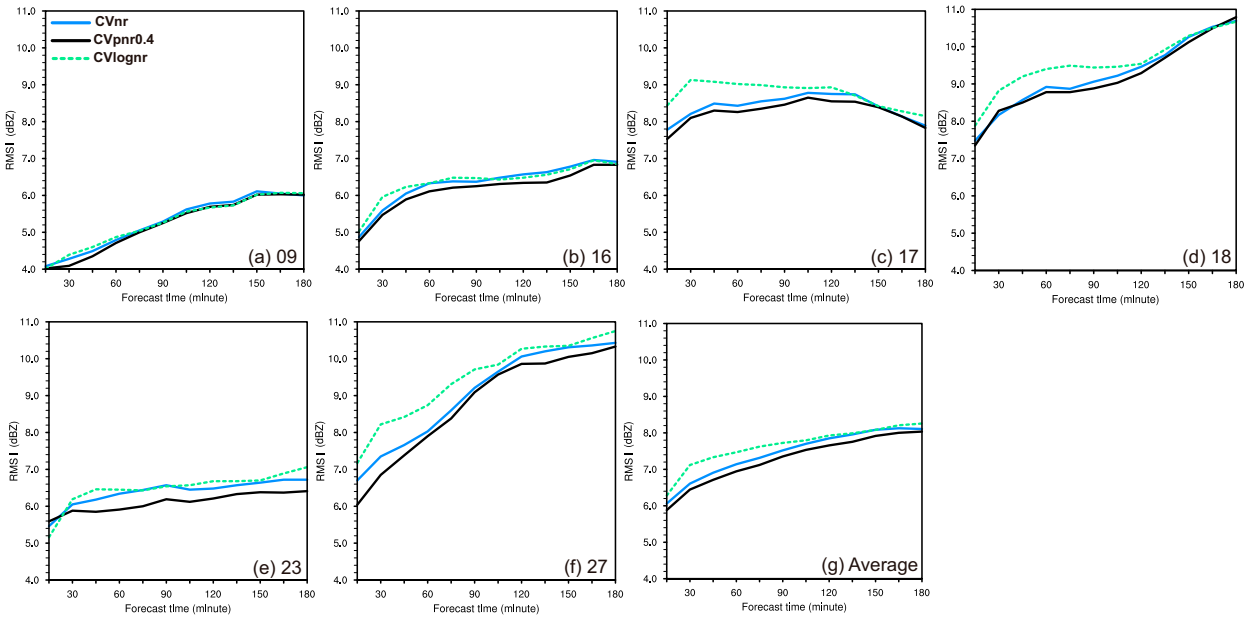

FIG. 16. RMSIs for predicted reflectivity of experiments CVnr (blue), CVpnr0.4 (black), and CVlognr (green) for the (a) 9, (b) 16, (c) 17, (d) 18, (e) 23, and (f) 27 May cases, and (g) the RMSIs averaged over the six cases from May 2017.

CVlognr. For other cases, the three methods show similar performance. According to all the scores, the performance of the 17 and 18 May cases is relatively better than that of the other cases. Figure 19g displays the statistical results aggregated across six cases for the 20-dBZ threshold. The three methods have similar scores at the first hour (circle marks). At the second hour (triangle marks), CVpnr0.4 has slightly higher POD, success ratio (SR, i.e., 1-FAR), and CSI while CVnr and CVlognr have similar scores. The differences among the three methods become more evident at the third hour (square marks). The POD, SR and CSI of CVpnr0.4 are the highest while those of CVlognr are the lowest. All three methods exhibit BIAS values of about 1.05 for all 3 h of the forecast, suggesting a little overprediction. In terms of the 45-dBZ threshold (Fig. 20), CVpnr0.4 and CVnr generally perform better than CVlognr. The aggregated results (Fig. 20g) show

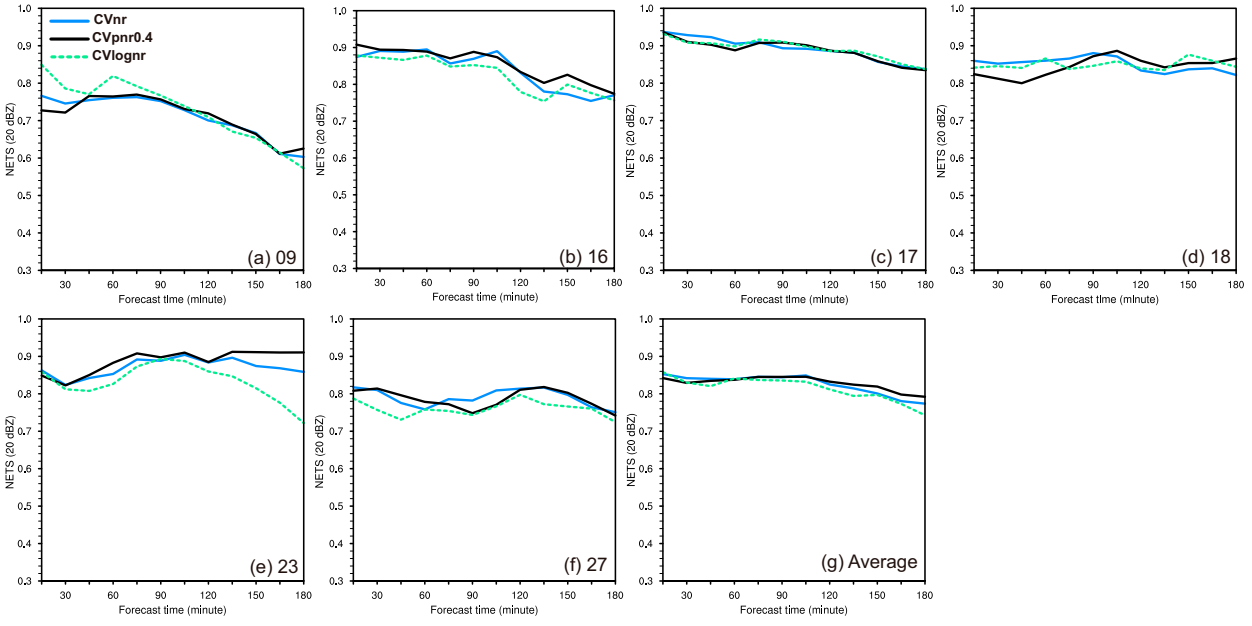

FIG. 17. NETSs for composite reflectivity forecasts of experiments CVnr (blue), CVpnr0.4 (black), and CVlognr (green) with the threshold of 20 dBZ for (a)–(f) six cases and (g) the NETSs averaged over six cases. The labels in (a)–(f) indicate the dates of the cases.

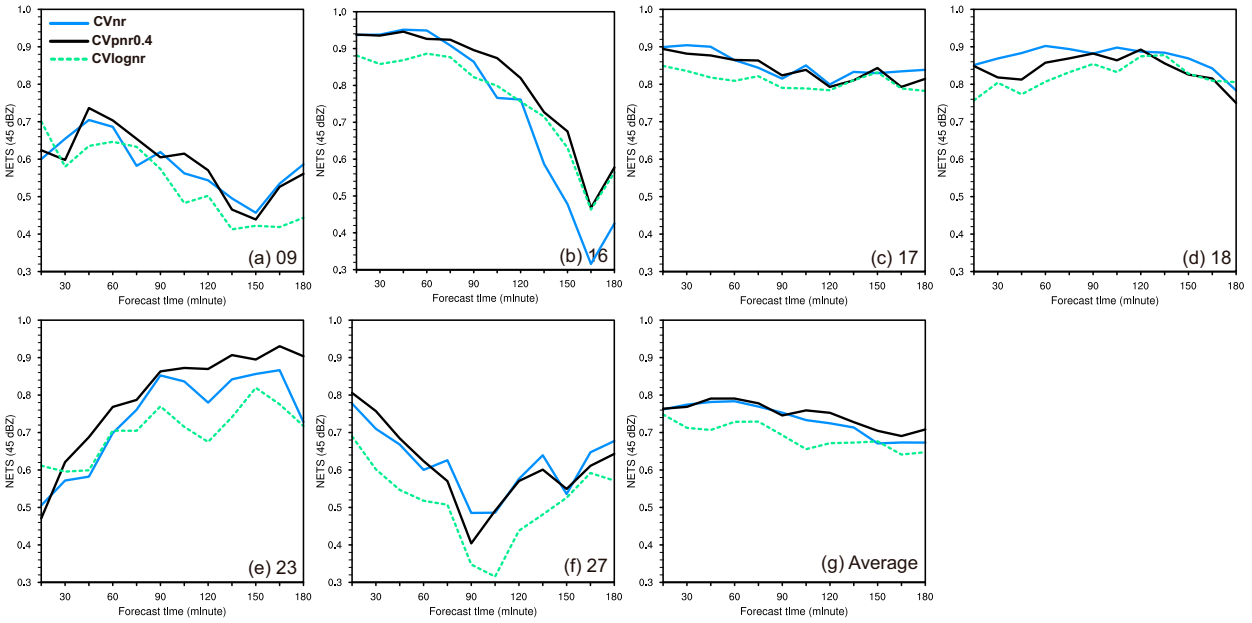

FIG. 18. As in Fig. 17, but for the threshold of 45 dB*Z*.

that all three methods have higher BIAS values (between 1.2 and 1.3) for all 3 h of forecasts, especially with CVlognr, implying more overprediction. At 1 h, the highest SR for CVpnr0.4, combined with a POD similar to those of CVnr and CVlognr, results in the high CSI score of ~0.8 for CVpnr0.4. In the later 2 h of the forecast, CVpnr0.4

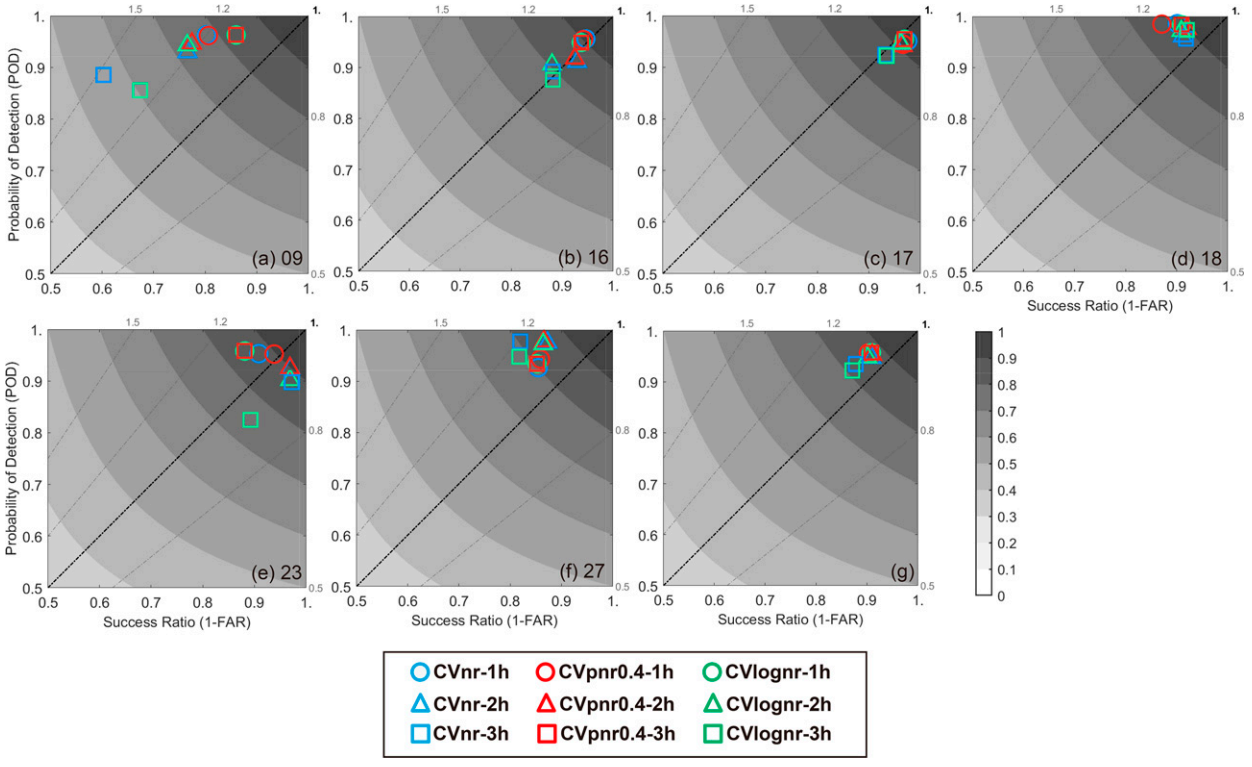

FIG. 19. Performance diagrams for composite reflectivity forecasts of experiments CVnr (blue), CVpnr0.4 (red), and CVlognr (green) with the threshold of 20 dB*Z* for (a)–(f) six cases, and (g) the statistical results generated from aggregating across six cases. The labels in (a)–(f) indicate the dates of the cases. Diagonal and curved lines represent lines of constant BIAS and CSI, respectively. Circle, triangle, and rectangle marks represent 1-, 2-, and 3-h forecasts, respectively.

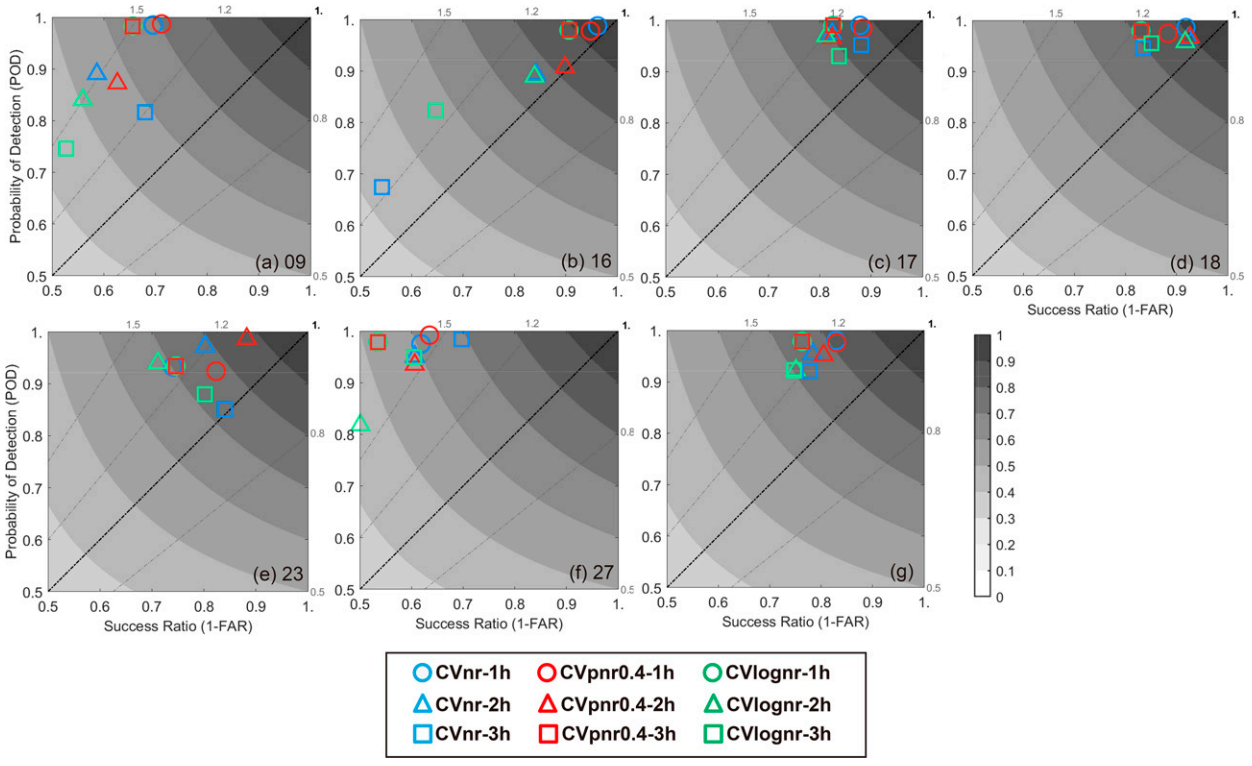

FIG. 20. As in Fig. 19, but for the threshold of 45 dBZ.

continues to have the highest CSI, with CVnr in the second, and CVlognr in the third.

Even though the predicted composite reflectivity of CVpnr0.4, CVnr, and CVlognr for the May 16 case has been subjectively evaluated and compared in Fig. 13, to further compare their performances for the other five cases, the 3-h predicted composite reflectivity fields are provided in Fig. 21. Consistent with the above discussions, CVlognr generally produces more spurious scattered echoes than CVpnr0.4 and CVnr, especially for the 17, 18, and 27 May cases (Figs. 21h,l,t). CVpnr0.4 and CVnr have overall similar results for the 9, 17, and 18 May cases. For the 23 May case, CVpnr0.4 predicts the storms in the middle of the domain more accurately (Fig. 21o) while CVnr and CVlognr have eastward displacement errors (Figs. 21n,p). For the 27 May case, CVnr produces more small spurious echoes in southwest Missouri (Fig. 21r).

To sum up, the evaluations of the predicted reflectivity for six cases further support the conclusion that CVpnr0.4 produces more skillful short-term forecasts than CVnr and CVlognr for convective storms.

5. Summary and conclusions

Radar DA is helpful in improving convective-scale numerical weather prediction. However, direct assimilation of reflectivity remains challenging in a variational framework because of the highly nonlinear reflectivity observation operator. When using a more advanced reflectivity observation operator based on a DM MP scheme (the Thompson scheme in our case), the inclusion of total number concentration for rainwater N_{tr} itself as the control variable (denoted as CVnr) may prevent efficient cost function minimization convergence due to the very large dynamic range of N_{tr} values and the highly nonlinear relationship between reflectivity and N_{tr}. Using logarithmic transformed N_{tr} as control variable (CVlognr) can help alleviate such a problem, but can also produce spuriously large analysis increments due to the highly nonlinear logarithmic transform. In this study, a generalized power transform function is applied to N_{tr} (CVpnr), in which the nonlinearity of transform can be adjusted by tuning the exponent parameter p.

The performances of CVnr, CVlognr, and CVpnr are first compared in great depth within GSI En3DVar framework through the analysis and forecast of the 16 May 2007 supercell case over Texas and Oklahoma. A set of cycled DA and 3-h forecast experiments is conducted using the generalized power transform with different parameters p (10^{-6}, 0.2, 0.4 0.6, 0.8 and 1.0). The optimal p value is found to be 0.4 in terms of overall lower RMSI and higher NETS for reflectivity forecasts. Later comparisons are focused on the use of CVnr, CVlognr and CVpnr with p set to 0.4 (CVpnr0.4).

Single-time analyses using the same background show that the convergence of cost function minimization in CVpnr0.4 and CVlognr is much faster than in CVnr because the nonlinearity between reflectivity and transformed N_{tr} is reduced by the transform. When using fewer iterations (3 outer-loop and 25 inner-loop iterations), the analyzed reflectivity of the intense storms in Oklahoma Panhandle and southwest Kansas (referred to as northern storms) has

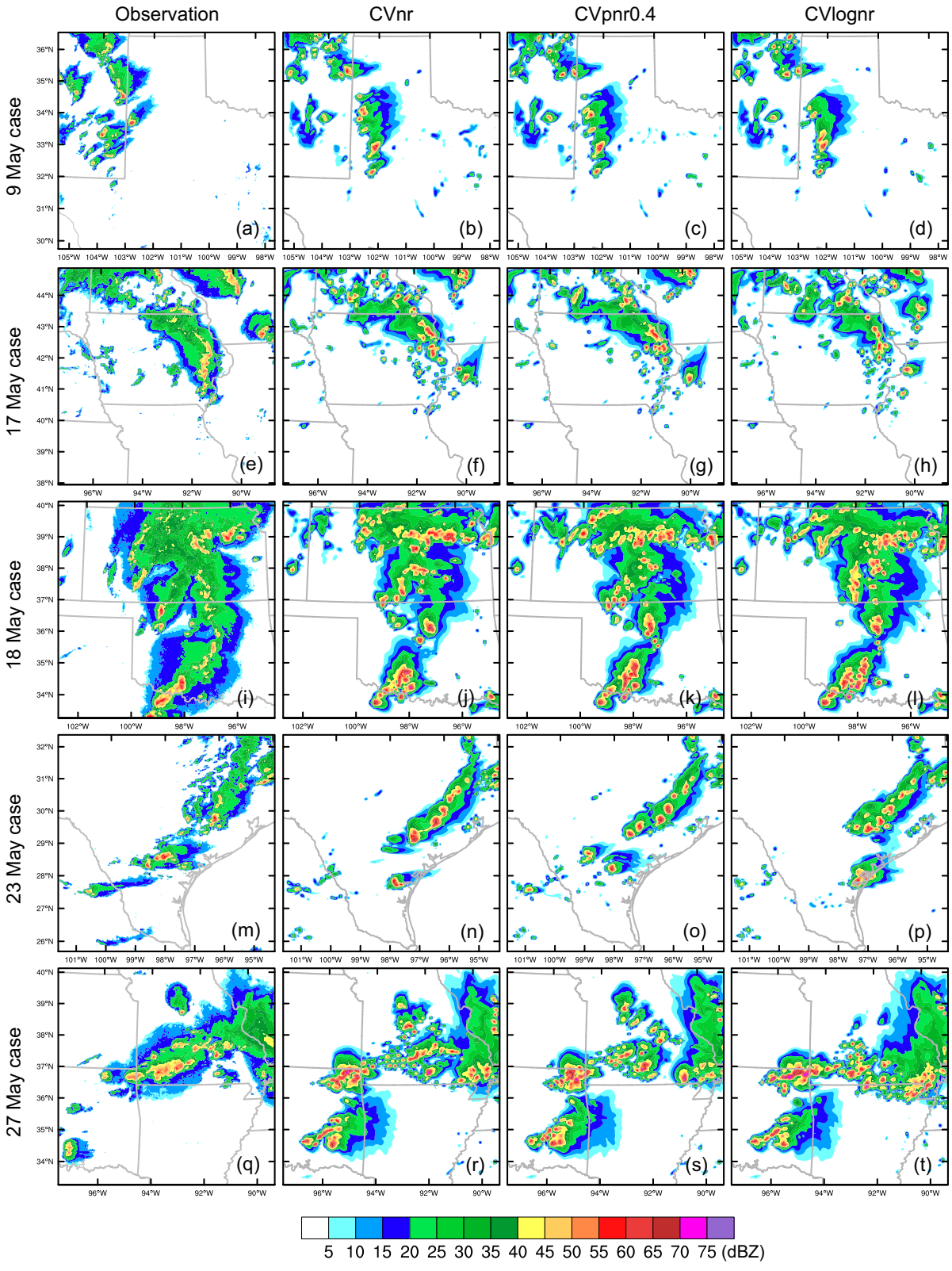

FIG. 21. The 3-h predicted composite reflectivity (dBZ) for the (b)–(d) 9 May, (f)–(h) 17 May, (j)–(l) 18 May, (n)–(p) 23 May, and (r)–(t) 27 May cases from the cycled data assimilation and forecast experiments CVnr, CVpnr0.4, and CVlognr, shown in columns from left to right. (a),(e),(i),(m),(q) The corresponding observed composite reflectivity.

somewhat less spatial coverage in CVnr while it is overestimated in CVlognr. The cost function value at the end of minimization is larger in CVnr because of its much slower convergence rate. CVlognr produces very large values of N_{tr} due to the large gradient of cost function with respect to the logarithmic transformed N_{tr}. Such too large values of N_{tr} appear to lead to large adjustments in the initial forecasts.

When greatly increasing iteration numbers (from 25 inner-loop and 3 outer-loop iterations to up to 200 inner-loop and 5 outer-loop iterations), the cost function value at the end of minimization is much reduced in CVnr and the quality of analyzed reflectivity is improved to some extent, but little impact is found on the analyses of CVpnr0.4 and CVlognr because reasonable convergence is already reached with the fewer number of iterations. The final analysis appears to mainly depend on the choice of control variable via its effect on the cost function gradient with respect to the control variable as long as reasonable convergence is reached.

CVnr, CVlognr, and CVpnr0.4 are also compared for the forecasts of composite reflectivity and hourly precipitation. Both CVnr and CVlognr produce more spurious echoes than CVpnr0.4 at the end of a total of 3-h-long DA cycles. Hourly precipitation in the later forecast hours is underpredicted in CVnr and more errors in the location and coverage of precipitation centers are found in CVlognr, especially in the southern part of the Texas Panhandle and western Oklahoma. Overall, the superior performance of CVpnr0.4 is demonstrated by qualitative and quantitative comparisons among the cycled DA and forecast experiments for the 16 May supercell case.

The performances of CVpnr0.4, CVnr, and CVlognr are further quantitatively evaluated using six thunderstorm cases from May 2017 via experiments using the same DA and forecast configurations. The statistical evaluation results further support the conclusion about the superior performance of CVpnr0.4. CVpnr0.4 has the smallest RMSIs of predicted reflectivity averaged over six cases. In terms of average NETS and performance diagram for reflectivity forecast, CVpnr0.4 presents comparable skill to CVnr during the early forecast period, and highest skill during the later forecast period, while CVlognr shows the poorest performance overall.

In Liu et al. (2022), the comparison between the newly developed DM-type Z operator with the CVnr method and the SM-type Z operator adopted in Chen et al. (2021) shows that using the DM-type Z operator is better for the analysis and forecast of convective storms than using the SM-type Z operator. This study further demonstrates that the CVpnr method with an optimal exponent parameter outperforms the CVnr method when using the DM-type Z operator to directly assimilate radar reflectivity. In short, using the DM-type Z operator with the CVpnr method in this study shows greater potential for further improving the convective scale short-term forecast.

Although some conclusions in this study should be general, such as those on the convergence rate of cost function minimization when different control variable formulation is used, the robustness of the conclusions on impacts on convective storm forecasts can benefit from testing with more cases from different regions and seasons. Qualitatively, our conclusions on the choice of the control variable should be sound, however.

Based on the Thompson MP scheme, the power transform applies to the number concentration of rainwater in this study. In the future, the power transform will be applied with fully three-moment MP schemes, and larger impact of the transform is expected when applied to number concentration of other hydrometeor species.

Acknowledgments. This research was supported by the NOAA Warn-on-Forecast (WoF) Grant NA16OAR4320115, NOAA Joint Technology Transfer Initiative (JTTI) Grant NA18OAR4590385, and the National Natural Science Foundation of China (Grant 41905047). Dr. Kent H. Knopfmeier of NSSL is thanked for providing the ensemble initial conditions and lateral boundary conditions data. Computational resources of the Oklahoma Supercomputing Center for Research and Education (OSCER), and the NSF Xsede Supercomputing Centers were used. The severe weather report data were downloaded from the website of the Storm Prediction Center of NOAA'S National Weather Service (https://www.spc.noaa.gov/climo/reports), and the NEXRAD level-2 radial velocity data were download from the website (https://www.ncdc.noaa.gov/nexradinv/index.jsp). Model data produced from this study have been archived at the Harvard data server (https://doi.org/10.7910/DVN/NPUKN7).

APPENDIX

List of Acronyms and Symbols

Table A1 briefly describes the acronyms and symbols used in the main text.

TABLE A1. List of acronyms and symbols.

Acronyms/ symbols	Description
BIAS	Frequency bias
CSI	Critical success index
CVlognr	Method using logarithmic N_{tr} as control variable when assimilating reflectivity
CVnr	Method using N_{tr} as control variable when assimilating reflectivity
CVpnr	Method using a general power transform of N_{tr} as control variable when assimilating reflectivity
DA	Data assimilation
FAR	False alarm ratio
GDn	Cost function gradient with respect to different forms of N_{tr}
GDq	Cost function gradient with respect to the power-transformed q_r
NETS	Neighborhood equitable threat score
N_{tr}	Total number concentration of rainwater
p	Adjustable exponent in the power transform function for N_{tr}
POD	Probability of detection
q_g	Graupel mixing ratio
q_r	Rainwater mixing ratio
q_s	Snow mixing ratio
RMSI	Root-mean-square innovation
Z	Radar reflectivity

REFERENCES

Brewster, K., M. Hu, M. Xue, and J. Gao, 2005: Efficient assimilation of radar data at high resolution for short-range numerical weather prediction. *World Weather Research Program Symp. on Nowcasting and Very Short-Range Forecasting*, WSN05, Tolouse, France, WMP, Paper 3.06.

Carley, J. R., 2012: Hybrid ensemble-3DVar radar data assimilation for the short-term prediction of convective storms. Ph.D. dissertation, Department of Earth, Atmospheric, and Planetary Sciences, Purdue University, 205 pp.

Chen, F., and J. Dudhia, 2001: Coupling an advanced land surface–hydrology model with the Penn State–NCAR MM5 modeling system. Part I: Model implementation and sensitivity. *Mon. Wea. Rev.*, **129**, 569–585, https://doi.org/10.1175/1520-0493(2001)129<0569:CAALSH>2.0.CO;2.

Chen, L., C. Liu, M. Xue, G. Zhao, R. Kong, and Y. Jung, 2021: Use of power transform mixing ratios as hydrometeor control variables for direct assimilation of radar reflectivity in GSI En3DVar and tests with five convective storms cases. *Mon. Wea. Rev.*, **149**, 645–659, https://doi.org/10.1175/MWR-D-20-0149.1.

Clark, A. J., W. A. Gallus, and M. L. Weisman, 2010: Neighborhood-based verification of precipitation forecasts from convection-allowing NCAR WRF model simulations and the operational NAM. *Wea. Forecasting*, **25**, 1495–1509, https://doi.org/10.1175/2010WAF2222404.1.

Dawson, D. T., II, and M. Xue, 2006: Numerical forecasts of the 15–16 June 2002 Southern Plains severe mesoscale convective system: Impact of mesoscale data and cloud analysis. *Mon. Wea. Rev.*, **134**, 1607–1629, https://doi.org/10.1175/MWR3141.1.

——, ——, J. A. Milbrandt, and M. K. Yau, 2010: Comparison of evaporation and cold pool development between single-moment and multi-moment bulk microphysics schemes in idealized simulations of tornadic thunderstorms. *Mon. Wea. Rev.*, **138**, 1152–1171, https://doi.org/10.1175/2009MWR2956.1.

de Pondeca, M. S., and Coauthors, 2011: The real-time mesoscale analysis at NOAA's National Centers for Environmental Prediction: Current status and development. *Wea. Forecasting*, **26**, 593–612, https://doi.org/10.1175/WAF-D-10-05037.1.

Dowell, D. C., F. Zhang, L. J. Wicker, C. Snyder, and N. A. Crook, 2004: Wind and temperature retrievals in the 17 May 1981 Arcadia, Oklahoma, supercell: Ensemble Kalman filter experiments. *Mon. Wea. Rev.*, **132**, 1982–2005, https://doi.org/10.1175/1520-0493(2004)132<1982:WATRIT>2.0.CO;2.

——, L. J. Wicker, and C. Snyder, 2011: Ensemble Kalman filter assimilation of radar observations of the 8 May 2003 Oklahoma City thunderstorm: Influences of reflectivity observations on storm-scale analyses. *Mon. Wea. Rev.*, **139**, 272–294, https://doi.org/10.1175/2010MWR3438.1.

——, and Coauthors, 2016: Development of a High-Resolution Rapid Refresh Ensemble (HRRRE) for severe weather forecasting. *28th Conf. on Severe Local Storms*, Portland, OR, Amer. Meteor. Soc., 8B.2, https://ams.confex.com/ams/28SLS/webprogram/Paper301555.html.

Evensen, G., 1994: Sequential data assimilation with a nonlinear quasi-geostrophic model using Monte Carlo methods to forecast error statistics. *J. Geophys. Res.*, **99**, 10 143–10 162, https://doi.org/10.1029/94JC00572.

——, 2003: The ensemble Kalman filter: Theoretical formulation and practical implementation. *Ocean Dyn.*, **53**, 343–367, https://doi.org/10.1007/s10236-003-0036-9.

Gao, J., and M. Xue, 2008: An efficient dual-resolution approach for ensemble data assimilation and tests with assimilated Doppler radar data. *Mon. Wea. Rev.*, **136**, 945–963, https://doi.org/10.1175/2007MWR2120.1.

——, and D. J. Stensrud, 2012: Assimilation of reflectivity data in a convective-scale, cycled 3DVAR framework with hydrometeor classification. *J. Atmos. Sci.*, **69**, 1054–1065, https://doi.org/10.1175/JAS-D-11-0162.1.

——, and ——, 2014: Some observing system simulation experiments with a hybrid 3DEnVAR system for storm-scale radar data assimilation. *Mon. Wea. Rev.*, **142**, 3326–3346, https://doi.org/10.1175/MWR-D-14-00025.1.

——, M. Xue, and D. J. Stensrud, 2013: The development of a hybrid-3DVAR algorithm for storm-scale data assimilation. *Adv. Meteor.*, **2013**, 512656, https://doi.org/10.1155/2013/512656.

Hamill, T. M., and C. Snyder, 2000: A hybrid ensemble Kalman filter–3D variational analysis scheme. *Mon. Wea. Rev.*, **128**, 2905–2919, https://doi.org/10.1175/1520-0493(2000)128<2905:AHEKFV>2.0.CO;2.

Hogan, R. J., 2007: A variational scheme for retrieving rainfall rate and hail reflectivity fraction from polarimetric radar. *J. Appl. Meteor. Climatol.*, **46**, 1544–1564, https://doi.org/10.1175/JAM2550.1.

Hong, S.-Y., Y. Noh, and J. Dudhia, 2006: A new vertical diffusion package with an explicit treatment of entrainment processes. *Mon. Wea. Rev.*, **134**, 2318–2341, https://doi.org/10.1175/MWR3199.1.

Hu, M., M. Xue, and K. Brewster, 2006: 3DVAR and cloud analysis with WSR-88D level-II data for the prediction of the Fort Worth, Texas, tornadic thunderstorms. Part I: Cloud analysis and its impact. *Mon. Wea. Rev.*, **134**, 675–698, https://doi.org/10.1175/MWR3092.1.

Iacono, M. J., J. S. Delamere, E. J. Mlawer, M. W. Shephard, S. A. Clough, and W. D. Collins, 2008: Radiative forcing by long–lived greenhouse gases: Calculations with the AER radiative transfer models. *J. Geophys. Res.*, **113**, D13103, https://doi.org/10.1029/2008JD009944.

Johnson, A., X. Wang, J. R. Carley, L. J. Wicker, and C. Karstens, 2015: A comparison of multiscale GSI-based EnKF and 3DVar data assimilation using radar and conventional observations for midlatitude convective-scale precipitation forecasts. *Mon. Wea. Rev.*, **143**, 3087–3108, https://doi.org/10.1175/MWR-D-14-00345.1.

Johnson, M., Y. Jung, D. Dawson, and M. Xue, 2016: Comparison of simulated polarimetric signatures in idealized supercell storms using two-moment bulk microphysics schemes in WRF. *Mon. Wea. Rev.*, **144**, 971–996, https://doi.org/10.1175/MWR-D-15-0233.1.

Jung, Y., M. Xue, G. Zhang, and J. M. Straka, 2008: Assimilation of simulated polarimetric radar data for a convective storm using the ensemble Kalman filter. Part II: Impact of polarimetric data on storm analysis. *Mon. Wea. Rev.*, **136**, 2246–2260, https://doi.org/10.1175/2007MWR2288.1.

——, ——, and ——, 2010a: Simulations of polarimetric radar signatures of a supercell storm using a two-moment bulk microphysics scheme. *J. Appl. Meteor. Climatol.*, **49**, 146–163, https://doi.org/10.1175/2009JAMC2178.1.

——, ——, and ——, 2010b: Simultaneous estimation of microphysical parameters and atmospheric state using simulated polarimetric radar data and an ensemble Kalman filter in the presence of an observation operator error. *Mon. Wea. Rev.*, **138**, 539–562, https://doi.org/10.1175/2009MWR2748.1.

——, ——, and M. Tong, 2012: Ensemble Kalman filter analyses of the 29–30 May 2004 Oklahoma tornadic thunderstorm using one- and two-moment bulk microphysics schemes, with verification against polarimetric radar data. *Mon. Wea. Rev.*, **140**, 1457–1475, https://doi.org/10.1175/MWR-D-11-00032.1.

Kessler, E., 1995: On the continuity and distribution of water substance in atmospheric circulations. *Atmos. Res.*, **38**, 109–145, https://doi.org/10.1016/0169-8095(94)00090-Z.

Kleist, D. T., and K. Ide, 2015: An OSSE-based evaluation of hybrid variational–ensemble data assimilation for the NCEP GFS. Part I: System description and 3D-hybrid results. *Mon. Wea. Rev.*, **143**, 433–451, https://doi.org/10.1175/MWR-D-13-00351.1.

——, D. F. Parrish, J. C. Derber, R. Treadon, W.-S. Wu, and S. Lord, 2009: Introduction of the GSI into the NCEP global data assimilation system. *Wea. Forecasting*, **24**, 1691–1705, https://doi.org/10.1175/2009WAF2222201.1.

Kong, R., M. Xue, and C. Liu, 2018: Development of a hybrid En3DVar data assimilation system and comparisons with 3DVar and EnKF for radar data assimilation with observing system simulation experiments. *Mon. Wea. Rev.*, **146**, 175–198, https://doi.org/10.1175/MWR-D-17-0164.1.

——, ——, ——, and Y. Jung, 2021: Comparisons of hybrid En3DVar with 3DVar, and EnKF for radar data assimilation: Tests with the 10 May 2010 Oklahoma Tornado outbreak. *Mon. Wea. Rev.*, **149**, 21–40, https://doi.org/10.1175/MWR-D-20-0053.1.

Labriola, J., N. Snook, Y. Jung, B. Putnam, and M. Xue, 2017: Ensemble hail prediction for the storms of 10 May 2010 in south-central Oklahoma using single- and double-moment microphysical schemes. *Mon. Wea. Rev.*, **145**, 4911–4936, https://doi.org/10.1175/MWR-D-17-0039.1.

——, ——, ——, and M. Xue, 2020: Evaluating ensemble Kalman filter analyses of severe hail storms on 8 May 2017 in Colorado: Effects of state variable updating and multi-moment microphysics schemes on state variable cross covariances. *Mon. Wea. Rev.*, **148**, 2365–2389, https://doi.org/10.1175/MWR-D-19-0300.1.

——, Y. Jung, L. Chengsi, and M. Xue, 2021: Evaluating forecast performance and sensitivity to the GSI EnKF data assimilation configuration for the 28–29 May 2017 mesoscale convective system case. *Wea. Forecasting*, **36**, 127–146, https://doi.org/10.1175/WAF-D-20-0071.1.

Lin, Y.-L., R. D. Farley, and H. D. Orville, 1983: Bulk parameterization of the snow field in a cloud model. *J. Climate Appl. Meteor.*, **22**, 1065–1092, https://doi.org/10.1175/1520-0450(1983)022<1065:BPOTSF>2.0.CO;2.

Liu, C., M. Xue, and R. Kong, 2019: Direct assimilation of radar reflectivity data using 3DVAR: Treatment of hydrometeor background errors and OSSE tests. *Mon. Wea. Rev.*, **137**, 17–29, https://doi.org/10.1175/MWR-D-18-0033.1.

——, ——, and ——, 2020: Direct variational assimilation of radar reflectivity and radial velocity data: Issues with nonlinear reflectivity operator and solutions. *Mon. Wea. Rev.*, **148**, 1483–1502, https://doi.org/10.1175/MWR-D-19-0149.1.

——, H. Li, M. Xue, Y. Jung, J. Park, L. Chen, R. Kong, and C. C. Tong, 2022: Use of a reflectivity operator based on double-moment Thompson microphysics for direct assimilation of radar reflectivity in GSI-based hybrid En3DVar. *Mon. Wea. Rev.*, in press, https://doi.org/10.1175/MWR-D-21-0040.1.

Lorenc, A. C., 2003: The potential of the ensemble Kalman filter for NWP—A comparison with 4D-VAR. *Quart. J. Roy. Meteor. Soc.*, **129**, 3183–3203, https://doi.org/10.1256/qj.02.132.

Milbrandt, J. A., and M. K. Yau, 2005: A multimoment bulk microphysics parameterization. Part I: Analysis of the role of the spectral shape parameter. *J. Atmos. Sci.*, **62**, 3051–3064, https://doi.org/10.1175/JAS3534.1.

Pan, Y., K. Zhu, M. Xue, X. Wang, M. Hu, S. G. Benjamin, S. S. Weygandt, and J. S. Whitaker, 2014: A GSI-based coupled EnSRF–En3DVar hybrid data assimilation system for the operational Rapid Refresh model: Tests at a reduced resolution. *Mon. Wea. Rev.*, **142**, 3756–3780, https://doi.org/10.1175/MWR-D-13-00242.1.

Putnam, B. J., M. Xue, Y. Jung, N. A. Snook, and G. Zhang, 2014: The analysis and prediction of microphysical states and polarimetric variables in a mesoscale convective system using double-moment microphysics, multi-network radar data, and the ensemble Kalman filter. *Mon. Wea. Rev.*, **142**, 141–162, https://doi.org/10.1175/MWR-D-13-00042.1.

Roebber, P. J., 2009: Visualizing multiple measures of forecast quality. *Wea. Forecasting*, **24**, 601–608, https://doi.org/10.1175/2008WAF2222159.1.

Schenkman, A., M. Xue, A. Shapiro, K. Brewster, and J. Gao, 2011: The analysis and prediction of the 8–9 May 2007 Oklahoma tornadic mesoscale convective system by assimilating WSR-88D and CASA radar data using 3DVAR. *Mon. Wea. Rev.*, **139**, 224–246, https://doi.org/10.1175/2010MWR3336.1.

Skinner, P. S., and Coauthors, 2018: Object-based verification of a prototype Warn-on-Forecast System. *Wea. Forecasting*, **33**, 1225–1250, https://doi.org/10.1175/WAF-D-18-0020.1.

Smith, T. M., and Coauthors, 2016: Multi-Radar Multi-Sensor (MRMS) severe weather and aviation products: Initial operating capabilities. *Bull. Amer. Meteor. Soc.*, **97**, 1617–1630, https://doi.org/10.1175/BAMS-D-14-00173.1.

Snook, N., M. Xue, and Y. Jung, 2011: Analysis of a tornadic mesoscale convective vortex based on ensemble Kalman filter assimilation of CASA X-band and WSR-88D radar data. *Mon. Wea. Rev.*, **139**, 3446–3468, https://doi.org/10.1175/MWR-D-10-05053.1.

——, ——, and ——, 2012: Ensemble probabilistic forecasts of a tornadic mesoscale convective system from ensemble Kalman filter analyses using WSR-88D and CASA radar data. *Mon. Wea. Rev.*, **140**, 2126–2146, https://doi.org/10.1175/MWR-D-11-00117.1.

Stensrud, D. J., and Coauthors, 2009: Convective-scale warn-on-forecast system. *Bull. Amer. Meteor. Soc.*, **90**, 1487–1499, https://doi.org/10.1175/2009BAMS2795.1.

Sun, J., and N. A. Crook, 1997: Dynamical and microphysical retrieval from Doppler radar observations using a cloud model and its adjoint. Part I: Model development and simulated data experiments. *J. Atmos. Sci.*, **54**, 1642–1661, https://doi.org/10.1175/1520-0469(1997)054<1642:DAMRFD>2.0.CO;2.

——, and ——, 1998: Dynamical and microphysical retrieval from Doppler radar observations using a cloud model and its adjoint. Part II: Retrieval experiments of an observed Florida convective storm. *J. Atmos. Sci.*, **55**, 835–852, https://doi.org/10.1175/1520-0469(1998)055<0835:DAMRFD>2.0.CO;2.

——, and Coauthors, 2013: Use of NWP for nowcasting convective precipitation: Recent progress and challenges. *Bull. Amer. Meteor. Soc.*, **95**, 409–426, https://doi.org/10.1175/BAMS-D-11-00263.1.

Thompson, G., R. M. Rasmussen, and K. Manning, 2004: Explicit forecasts of winter precipitation using an improved bulk

microphysics scheme. Part I: Description and sensitivity analysis. *Mon. Wea. Rev.*, **132**, 519–542, https://doi.org/10.1175/1520-0493(2004)132<0519:EFOWPU>2.0.CO;2.

——, P. R. Field, R. M. Rasmussen, and W. D. Hall, 2008: Explicit forecasts of winter precipitation using an improved bulk microphysics scheme. Part II: Implementation of a new snow parameterization. *Mon. Wea. Rev.*, **136**, 5095–5115, https://doi.org/10.1175/2008MWR2387.1.

Tong, M., and M. Xue, 2005: Ensemble Kalman filter assimilation of Doppler radar data with a compressible nonhydrostatic model: OSS experiments. *Mon. Wea. Rev.*, **133**, 1789–1807, https://doi.org/10.1175/MWR2898.1.

——, and ——, 2008: Simultaneous estimation of microphysical parameters and atmospheric state with radar data and ensemble Kalman filter. Part II: Parameter estimation experiments. *Mon. Wea. Rev.*, **136**, 1649–1668, https://doi.org/10.1175/2007MWR2071.1.

Tong, C.-C., Y. Jung, M. Xue, and C. Liu, 2020: Direct assimilation of radar data with ensemble Kalman filter and hybrid ensemble-variational method in the National Weather Service operational data assimilation system GSI for the standalone regional FV3 model at a convection-allowing resolution. *Geophy. Res. Lett.*, **47**, e2020GL090179, https://doi.org/10.1029/2020GL090179.

Wang, H., J. Sun, S. Fan, and X.-Y. Huang, 2013: Indirect assimilation of radar reflectivity with WRF 3D-Var and its impact on prediction of four summertime convective events. *J. Appl. Meteor. Climatol.*, **52**, 889–902, https://doi.org/10.1175/JAMC-D-12-0120.1.

Wang, X., C. Snyder, and T. M. Hamill, 2007: On the theoretical equivalence of differently proposed ensemble-3DVAR hybrid analysis schemes. *Mon. Wea. Rev.*, **135**, 222–227, https://doi.org/10.1175/MWR3282.1.

Wang, Y., and X. Wang, 2017: Direct assimilation of radar reflectivity without tangent linear and adjoint of the nonlinear observation operator in the GSI-based EnVar system: Methodology and experiment with the 8 May 2003 Oklahoma City tornadic supercell. *Mon. Wea. Rev.*, **145**, 1447–1471, https://doi.org/10.1175/MWR-D-16-0231.1.

——, J. Gao, P. S. Skinner, K. Knopfmeier, T. Jones, G. Creager, P. L. Heiselman, and L. J. Wicker, 2019: Test of a weather-adaptive dual-resolution hybrid warn-on-forecast analysis and forecast system for several severe weather events. *Wea. Forecasting*, **34**, 1807–1827, https://doi.org/10.1175/WAF-D-19-0071.1.

Wheatley, D. M., K. H. Knopfmeier, T. A. Jones, and G. J. Creager, 2015: Storm-scale data assimilation and ensemble forecasting with the NSSL experimental warn-on-forecast system. Part I: Radar data experiments. *Wea. Forecasting*, **30**, 1795–1817, https://doi.org/10.1175/WAF-D-15-0043.1.

Xue, M., D.-H. Wang, J.-D. Gao, K. Brewster, and K. K. Droegemeier, 2003: The Advanced Regional Prediction System (ARPS), storm-scale numerical weather prediction and data assimilation. *Meteor. Atmos. Phys.*, **82**, 139–170, https://doi.org/10.1007/s00703-001-0595-6.

——, Y. Jung, and G. Zhang, 2010: State estimation of convective storms with a two-moment microphysics scheme and an ensemble Kalman filter: Experiments with simulated radar data. *Quart. J. Roy. Meteor. Soc.*, **136**, 685–700, https://doi.org/10.1002/qj.593.

Yang, R., R. J. Purser, J. R. Carley, M. de Pondeca, Y. Zhu, and S. Levine, 2020: Application of a nonlinear transformation function to the variational analysis of visibility and ceiling height. NOAA/NCEP Office Note 502, 210 pp., https://doi.org/10.25923/esw8-5n84.

Yussouf, N., and D. J. Stensrud, 2010: Impact of phased-array radar observations over a short assimilation period: Observing system simulation experiments using an ensemble Kalman filter. *Mon. Wea. Rev.*, **138**, 517–538, https://doi.org/10.1175/2009MWR2925.1.

——, E. R. Mansell, L. J. Wicker, D. M. Wheatley, and D. J. Stensrud, 2013: The ensemble Kalman filter analyses and forecasts of the 8 May 2003 Oklahoma City tornadic thunderstorm storm using single- and double-moment microphysics schemes. *Mon. Wea. Rev.*, **141**, 3388–3412, https://doi.org/10.1175/MWR-D-12-00237.1.